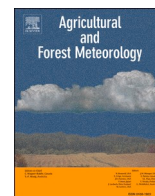


Contents lists available at [ScienceDirect](https://www.sciencedirect.com)

Agricultural and Forest Meteorology

journal homepage: www.elsevier.com/locate/agrformet

Peak growing season patterns and climate extremes-driven responses of gross primary production estimated by satellite and process based models over North America

Wei He^{a,b}, Weimin Ju^{a,b,*}, Fei Jiang^{a,b,*}, Nicholas Parazoo^c, Pierre Gentine^{d,e}, Xiaocui Wu^f, Chunhua Zhang^g, Jiawen Zhu^h, Nicolas Viovyⁱ, Atul K. Jain^j, Stephen Sitch^k, Pierre Friedlingstein^l

^a International Institute for Earth System Science, Nanjing University, Nanjing, Jiangsu 210023, China

^b Jiangsu Provincial Key Laboratory of Geographic Information Science and Technology, Key Laboratory for Land Satellite Remote Sensing Applications of Ministry of Natural Resources, School of Geography and Ocean Science, Nanjing University, Nanjing, Jiangsu 210023, China

^c Jet Propulsion Laboratory, California Institute of Technology, Pasadena, CA, USA

^d Department of Earth and Environmental Engineering, Columbia University, New York, 10027, USA

^e Columbia Water Center, Columbia University, New York, 10027, USA

^f Department of Microbiology and Plant Biology, Center for Spatial Analysis, University of Oklahoma, Norman, OK 73019, USA

^g School of Resources and Environmental Engineering, Ludong University, Yantai, 264000, China

^h International Center for Climate and Environment Sciences, Institute of Atmospheric Physics, Chinese Academy of Sciences, Beijing, China

ⁱ Laboratoire des Sciences du Climat et de l'Environnement, CEA CNRS UVSQ, 91191 Gif-sur-Yvette, France

^j Department of Atmospheric Sciences, University of Illinois, Urbana, IL 61801, USA

^k College of Life and Environmental Sciences, University of Exeter, Exeter, UK

^l College of Engineering, Mathematics and Physical Sciences, University of Exeter, Exeter, UK

A B S T R A C T

Representations of the seasonal peak uptake of CO₂ and climate extremes effects have important implications for accurately estimating annual magnitude and inter-annual variations of terrestrial carbon fluxes, however the consistency of such representations among different satellite models and process-based (PB) models remain poorly known. Here we investigated these issues over North America based on a large ensemble of state-of-the-art gross primary production (GPP) models, including two solar-induced chlorophyll fluorescence (SIF)-based models (WECANN and GOPT), three remote sensing driven light-use efficiency (LUE) models, and 10 PB models. We found that the two SIF-based GPP estimates were bilaterally consistent in spatial patterns of peak growing season GPP (GPP_{PGS}; with the largest uptake at the Corn-Belt area in the United States) and climate extremes-driven responses. The simulations from three LUE models showed relatively consistent spatial patterns of GPP_{PGS} and climate extremes-driven responses, which agreed well with SIF-based estimates and satellite based metrics. Obviously differed from SIF and LUE based estimates, the simulations from PB models exhibited noticeable divergences and mostly failed to reasonably replicate the spatial pattern of GPP_{PGS}. In addition, satellite models and PB models were comparably able to capture the effects of climate extremes on GPP, but showing obvious divergences in the magnitude of impacts among different models, and the former outperformed the latter in locating GPP changes caused by climate extremes. We discussed the possible origins of such discrepancies in state-of-the-art models with focus on PB models. Improving the parameterizations of critical variables (e.g. leaf area index) and better characterizing environmental stresses could lead to more robust estimates of large-scale terrestrial GPP with PB models, thus serving for accurately assessing global carbon budget and better understanding the impacts of climate change on the terrestrial carbon cycle. Our study offers a baseline for improving large-scale estimation of terrestrial GPP.

1. Introduction

Gross primary production (GPP) is the largest flux in the global terrestrial carbon cycle. To date, there are still large uncertainties in the annual magnitude and interannual variations (IAV) of estimated GPP at

the global scale (Chang et al., 2017; Huntzinger et al., 2012; Ito et al., 2016; Ito et al., 2017), and the uncertainties are even larger when looking into different regions and ecosystem types (Hilton et al., 2017; Hilton et al., 2015). The reliability of annual total GPP and its IAV estimated by carbon cycle models depends largely on their ability to

* Correspondence authors.

E-mail addresses: juweimin@nju.edu.cn (W. Ju), jiangf@nju.edu.cn (F. Jiang).

<https://doi.org/10.1016/j.agrformet.2020.108292>

Received 8 May 2020; Received in revised form 13 December 2020; Accepted 17 December 2020

Available online 25 December 2020

0168-1923/© 2020 Elsevier B.V. All rights reserved.

capture GPP in the peak growing season (PGS, a peak period of growing season, usually from June to August in the Northern Hemisphere) and responses to climate extremes. GPP in PGS (GPP_{PGS}) is much higher than in other seasons and predominantly determines the annual total. Observations suggested that seasonal peak GPP strongly influences IAV of GPP and net carbon balance (Reichstein et al., 2014; Xia et al., 2017). Climate extremes significantly affect carbon sequestration through photosynthesis processes and control IAV of GPP (Zscheischler et al., 2014). Therefore, it is a prerequisite to capture GPP in PGS and its responses to climate extremes for accurately characterizing the spatio-temporal variations of terrestrial carbon fluxes.

Due to the important role of GPP_{PGS} in annual carbon uptake, relevant issues have received intensive attentions (Huang et al., 2018; Wang et al., 2020a; Xia et al., 2017; Zhou et al., 2016). A recent study (Hilton et al., 2017) reported that the largest GPP_{PGS} for North America locates in the Corn-Belt area of Midwest US based on the best estimation of GPP, which was determined using aircraft atmospheric carbonyl sulfide (OCS) measurements. This agrees with the spatial pattern revealed by satellite solar-induced chlorophyll fluorescence (SIF) observations (Guanter et al., 2014). However, numerous biosphere models fail to capture this strong GPP spatial gradient (Guanter et al., 2014; Hilton et al., 2017), indicating that more efforts are required for investigating differences in spatial patterns of GPP_{PGS} estimated by different models.

In past decades, most model studies pay much attention to the mean states of terrestrial carbon fluxes at continental and regional scales (Chang et al., 2017; Huntzinger et al., 2012; Ito et al., 2016; Ito et al., 2017). However, few studies focus on effects of climate extremes on carbon fluxes (Schewe et al., 2019; Wu et al., 2018). How well models represent the response of terrestrial carbon fluxes to climate extremes is an important issue for model development. It urgently needs to shift our research efforts away from mean conditions towards extremes (Schewe et al., 2019), especially under the context of global climate change.

Process-based (PB) terrestrial biosphere models are commonly used for estimating historical GPP and projecting future status at regional and global scales. Such models, including diagnostic models (e.g. the Boreal Ecosystem Productivity Simulator (BEPS; Ju et al., 2006; Liu et al., 1997) and prognostic models (e.g. the Joint UK Land Environment Simulator (JULES; Clark et al., 2011; Slevin et al., 2017), are useful tools for understanding the mechanisms of terrestrial carbon cycling and its interactions with climate change. Although most PB models are designed for future projections, they are also popularly used to quantify historical carbon fluxes, e.g. for supporting the global carbon budget assessment (Global Carbon Project; Friedlingstein et al., 2019) and assessing climate extreme impacts (He et al., 2018; Li et al., 2019). However, PB models suffer from various uncertainties (Friedlingstein et al., 2006; Huntzinger et al., 2012), including model structure, parameterization, and inaccuracies in meteorological drivers and other input data (Huntzinger et al., 2017; Li et al., 2017; Rogers et al., 2017; Wu et al., 2017), which would bias flux estimates and hampered our understanding on the terrestrial carbon cycle. Thus, it is of great importance to benchmark model uncertainties with various sources of data and approaches.

Complemented to PB models, satellite-based models provide observation-constrained estimates of terrestrial carbon fluxes. Light-use efficiency (LUE) models (e.g. Vegetation Photosynthesis Model (VPM; Xiao et al., 2004; Zhang et al., 2017)), as one kind of satellite-based models, are usually formulated in a much simpler form and more readily driven by satellite data than PB models. In a recent decade, known as a useful proxy for photosynthesis (Guanter et al., 2014; Wood et al., 2017; Zhang et al., 2016a), SIF retrieved from multiple satellite platforms has been employed to constrain global GPP estimates (Alemohammad et al., 2017; MacBean et al., 2018; Norton et al., 2019; Parazoo et al., 2014) and to validate model-based GPP estimates (Byrne et al., 2018; Zan et al., 2018; Zhang et al., 2016b). SIF has been proved to be effective in tracking the spatiotemporal dynamic of GPP and detecting its environmental stresses (Song et al., 2018; Sun et al., 2015;

Wang et al., 2020b). These satellite-based models or methods may provide an important perspective for understanding the terrestrial carbon cycle under the context of climate change based on historical simulations and discerning potential uncertainties in PB models.

North America is an area with intensive carbon cycle observation data, e.g. eddy covariance measurements, crop yield inventory, SIF, and atmospheric OCS measurements, which makes it an ideal region for studying the terrestrial carbon cycle. In addition, the recent climate extreme events (e.g. the 2011 and 2012 droughts) in North America offer an opportunity to examine and evaluate model capacity for simulating impacts of climate extremes on GPP. Although several studies have carried out GPP model inter-comparison studies over North America (e.g., Huntzinger et al., 2012; Schaefer et al., 2012), most focused on the mean annual total, mean annual spatial pattern, and mean seasonal and inter-annual variations of fluxes. Here we focus on examining the spatial patterns of GPP_{PGS} and extreme climate-driven responses of GPP, which are important aspects of model performance. With the advent of new satellite-based models for GPP estimates, e.g. SIF-based models (WECANN and GOPT), the investigation regarding to the consistency between satellite-based models (newly SIF-based and traditionally LUE-based) and PB models would be of great importance for enlightening model developments, as well as interpreting satellite signals.

In this study, based on a large ensemble of satellite models (SIF-based and LUE-based) and PB models, we aim to answer two questions: (1) Can satellite (SIF-based and LUE-based) and PB models reasonably reproduce the typical mean-state spatial pattern of GPP_{PGS} over North America (the largest uptake in Corn-Belt area) as uncovered by the satellite SIF and atmospheric OCS data? (2) Can satellite and PB models be able to accurately capture the impacts of climate extremes on GPP?

2. Data and methods

2.1. SIF-based GPP estimates

2.1.1. WECANN GPP

The Water, Energy, and Carbon with Artificial Neural Networks (WECANN) product (Alemohammad et al., 2017) provides monthly latent heat, sensible heat, and GPP estimates from 2007 to 2015 at a spatial resolution of $1^\circ \times 1^\circ$. WECANN retrieves these variables using an artificial neural network (ANN) driven by remotely sensed SIF in conjunction with other data sources, including precipitation, air temperature, soil moisture, snow cover, and net radiation. A target data set generated from three independent data sources, MODIS (Moderate-Resolution Imaging Spectroradiometer) GPP, ECMWF (European Centre for Medium-Range Weather Forecasts), and FLUXNET-MTE (Model Tree Ensembles), weighted using a triple collocation algorithm, was used for training neural network. Validations with FLUXNET flux and other data sets proved that WECANN GPP performs well on indicating seasonal variations, spatial patterns and extreme heatwave and drought impacts (Gentine and Alemohammad, 2018).

2.1.2. GOPT GPP

GPP optimal estimation (GOPT) data is produced through the combination of the satellite SIF data and prior estimates from the TRENDY (Trends in the land carbon cycle) models using a data assimilation approach (Parazoo et al., 2014). In this study, we used the GOPT GPP derived from the Global Ozone Monitoring Experiment-2 (GOME-2) SIF data (Joiner et al., 2011) and the prior from the ensemble mean of 10 TRENDY (v2) models at the spatial resolution of $1^\circ \times 1^\circ$ on a monthly basis. It has been validated against flux tower measurements from FLUXNET and shows favorable global performance. For more details on this data set refer to Parazoo et al. (2014). GOPT has been used to examine large-scale GPP patterns and regional carbon cycle responses to climate extremes (Bowman et al., 2017; Liu et al., 2017a; Parazoo et al., 2015; Parazoo et al., 2014).

2.2. FLUXCOM GPP

The FLUXCOM GPP product (www.fluxcom.org) is produced by upscaling FLUXNET flux measurements. The upscaling process uses machine learning (ML) algorithms (Jung et al., 2017; Tramontana et al., 2016) to scale in-situ flux measurements into time-resolved $0.5^\circ \times 0.5^\circ$ grids of net ecosystem productivity (NEP), ecosystem respiration (Reco) and GPP for the period 1980–2013 using meteorological data and mean seasonal cycles of remotely sensed data. Meteorological variables were retrieved from the CRUNCEP v6 data set. The pattern of plant functional types originates from the majority classes of annually resolved MODIS land cover product (collection 5) (Friedl et al., 2010). The daily fluxes were aggregated to monthly values. Predictions of GPP and Reco fluxes were produced with three different ML algorithms in the version FLUXCOM RS+METEO, including ANN, multivariate adaptive regression splines, and random forests, and two methods used for separating GPP and Reco from tower-based NEP (Lasslop et al., 2010; Reichstein et al., 2005). Thus, there are 6 sets of GPP and Reco, respectively. In this study, we used the means and standard deviations of different GPP data sets over the period from 2007 to 2013.

2.3. GPP from light-use efficiency models

LUE models calculate GPP as the product of incident photosynthetically active radiation (PAR), fraction of absorbed PAR (fPAR), maximum light use efficiency (ϵ_0), and scalars of environmental variables (Monteith, 1972; Monteith, 1977):

$$\text{GPP} = \text{PAR} \times \text{fPAR} \times \epsilon_0 \times f(T) \times f(W) \quad (1)$$

where $f(T)$ and $f(W)$ are the scalars of temperature and moisture, respectively.

Different LUE models share the same basic structure above, but have different fPAR and different parametrizations of the LUE factors: ϵ_0 , $f(T)$, and $f(W)$. This study uses GPP estimated from three different LUE models, including the Carnegie-Ames-Stanford Approach (CASA), the Vegetation Photosynthesis Model (VPM), and the MOD17 GPP algorithm. The major characteristics of these LUE models are summarized in Table S1.

The CASA model was originally developed by Potter et al. (1993) and improved since Randerson et al. (1996). The version we used here is CASA-GFED3 (Global Fire Emissions Database, Version 3), following Van der Werf et al. (2010). In CASA, GPP is assumed to be twice net primary production (NPP), which is estimated using equation (1). Meteorological forcing data are taken from the Global Modeling and Assimilation Office's (GMAO) Modern-Era Retrospective Analysis for Research and Applications (MERRA, <http://gmao.gsfc.nasa.gov/merra/>; Rienecker et al. (2011)). fPAR is estimated from AVHRR NDVI and vegetation classification is according to the MODIS MOD12Q1 product. The LUE parameters in the CASA-GFED3 model have been calibrated against Midwestern USA crop yields (Hilton et al., 2015; Lobell et al., 2002). The CASA-GFED3 data set was downloaded from <https://nacp-files.nacarbon.org/nacp-kawa-01/>.

The VPM model was developed by Xiao et al. (2004). The most important features of this model include considering the influence of both maximum and minimum temperatures on GPP and quantifying the impact of soil moisture on GPP using Land Surface Water Index (LSWI), which is determined according to remotely sensed reflectance of near and short-wave infrared bands. We used monthly GPP data produced by Zhang et al. (2017) (<https://doi.org/10.6084/m9.figshare.c.3789814>) over the period from 2000 to 2016. In the production of GPP, the National Center for Environmental Prediction reanalysis data set (NCEP-reanalysis II) was used to drive the VPM model. It is worth noting that the model differentiates C3/C4 difference for crops, savannas, grass, wetland, and cropland/natural vegetation when parameterizing ϵ_0 (Zhang et al., 2017).

The MOD17 algorithm produces 8-day GPP with satellite-derived fPAR from MOD15 and GMAO/NASA (National Aeronautics and Space Administration) meteorological data. Biome-specific parameter values are derived empirically from BIOME-BGC model simulations (Running et al., 2004; White et al., 2000). The values of ϵ_0 vary widely with vegetation types. For more details refer to Running and Zhao (2015). In this study, we used the latest version of MODIS 8-day GPP product (version MOD17A2H) over the period from 2000 to 2016 (<https://ladsweb.modaps.eosdis.nasa.gov>). The 8-day GPP was aggregated into monthly values.

2.4. GPP from process-based models

The GPP simulated by 10 process models, covering both prognostic and diagnostic models, was used for the analysis. Among them, 8 models are global dynamic vegetation models, which participated in the TRENDY project (Sitch et al., 2015), including ORCHIDEE (Krinner et al., 2005), ORCHIDEE-MICT (Guimberteau et al., 2018); CABLE (Wang et al., 2010), DLEM (Tian et al., 2015), ISAM (Jain et al., 2013), VEGAS (Zeng et al., 2005), VISIT (Kato et al., 2013) and JULES (Clark et al., 2011). Here we used the outputs from TRENDY version 6 under the simulation scenario S3, which accounts for the effects of CO₂ fertilization, climate, and land use change on GPP. Models were forced using the CRUNCEP v8 data set (https://vesg.ipsl.upmc.fr/thredds/catalog/store/p529viov/cruncep/V8_1901_2016/catalog.html). The simulation by JULES provided monthly GPP at a resolution of $1.875^\circ \times 1.25^\circ$, the simulation by ORCHIDEE-MICT provided monthly GPP at a resolution of $1^\circ \times 1^\circ$, and the other simulations provided GPP at a spatial resolution of $0.5^\circ \times 0.5^\circ$.

In order to investigate the impact of vegetation phenology representation on simulated GPP, we also included the GPP simulations from two diagnostic process models, SiBCASA model (Schaefer et al., 2008; van der Velde et al., 2014) and BEPS model (Ju et al., 2006; Liu et al., 1997). Different from above prognostic models, these two diagnostic models were driven using remotely sensed normalized difference vegetation index (NDVI) or leaf area index (LAI), which represents the vegetation phenology in models. The SiBCASA model was driven by NDVI (used to derive fPAR and LAI) and ECMWF meteorological data (van der Velde et al., 2014). The BEPS model was driven by two different remotely sensed LAI data sets, GLOBMAP v3 (named as BEPS-R1) and GLASS AVHRR LAI (named as BEPS-R2), and meteorological data from CRUNCEP v7. The reason for using two LAI products is to investigate the uncertainty of LAI on simulated GPP in PB models (here BEPS as a testing model). These LAI products are described in more details in Section 2.6.4.

2.5. Climate data

The impacts of water and temperature anomalies on GPP were assessed using monthly air temperature and precipitation at a spatial resolution of $0.5^\circ \times 0.5^\circ$ from the CRUNCEP v6 data set produced by the Institute Pierre Simon Laplace (IPSL) of France (Wei et al., 2014). The CRUNCEP v6 data set is a merged product of Climate Research Unit observation-based monthly $0.5^\circ \times 0.5^\circ$ climate variables (New et al., 2000) (1901–2014) and the 6-hourly reanalysis of National Centers for Environmental Prediction (NCEP). This data set is also the meteorological driver of the FLUXCOM, BEPS and TRENDY models.

2.6. Satellite land surface variables

2.6.1. Soil moisture

The impact of soil moisture stress on GPP was investigated using the Global Land-surface Evaporation Amsterdam Methodology (GLEAM) root-zone soil moisture (SM). GLEAM root-zone SM is produced from the satellite surface soil moisture product ESA-CCI SM (v02.5) through a data assimilation scheme (Martens et al., 2017; Miralles et al., 2011).

ESA-CCI SM is a satellite surface soil moisture product (within the upmost 5 centimeters of soils) from the European Space Agency Climate Change Initiative and an Essential Climate Variable, which is a combination of passive (SMMR, SSM/I, TMI, AMSR-E, WindSat, AMSR2, and SMOS) and active (AMI-WS and MetOp A/B ASCAT) microwave products with a spatial resolution of $0.25^\circ \times 0.25^\circ$ (Dorigo et al., 2017). The validation against in-situ measurements by many studies proved the high quality of ESA-CCI SM (Dorigo et al., 2015; Peng et al., 2015).

2.6.2. Solar-induced chlorophyll fluorescence

Remotely sensed SIF has shown great promise for tracking spatio-temporal variations of GPP (Guanter et al., 2014; Zhang et al., 2016a) and is also sensitive to water (Alden et al., 2016; Lee et al., 2013; Sun et al., 2015) and temperature stresses (Song et al., 2018). The monthly SIF at 740 nm with a spatial resolution of $0.5^\circ \times 0.5^\circ$ (version 27) retrieved from GOME-2 (Joiner et al., 2013) was used to indicate the response of GPP to water or temperature stresses.

2.6.3. Enhanced vegetation index

The enhanced vegetation index (EVI; MOD13C1) from the MODIS data was also used to assess the vegetation response to droughts and temperature anomalies. This 16-day composite data set at a spatial resolution of $0.05^\circ \times 0.05^\circ$ was calculated using the MODIS/Terra reflectance (v6) data (Huete et al., 2002). A Savitzky–Golay filter built in the TIMESAT 3.2 software (Jönsson and Eklundh, 2004) was applied to fill gaps of low-quality data.

2.6.4. Leaf area index

Two satellite LAI products, GLOBMAP LAI (v3) and GLASS LAI, were used for investigating the impact of LAI on GPP simulations by PB models.

GLOBMAP LAI (v3) provides a consistent long-term global LAI product (1981–2016) at a spatial resolution of 8 km with a geographic latitude/longitude projection generated through pixelwise fusion of the Advanced Very High Resolution Radiometer (AVHRR) NDVI (1981–1999) and LAI inverted from MODIS reflectance data (2000–2016) (Liu et al., 2012).

The Global Land Surface Satellite (GLASS) LAI product was generated using general regression neural networks (GRNNs), in which the reprocessed remote sensing reflectance values from an entire year were inputted to the GRNNs to estimate the one-year LAI profile. The GLASS LAI retrievals are separately derived from MODIS reflectance data (named GLASS MODIS) and from the Long-Term Data Record (LTDR) AVHRR reflectance data (named as GLASS AVHRR). The GLASS MODIS LAI product is provided in a sinusoidal projection at a spatial resolution of 1 km and spans from 2000 to 2015, while the latest version of the GLASS AVHRR LAI product is provided in a geographic latitude/longitude projection at a spatial resolution of 0.05° and spans from 1981 to 2015. In this study, we used the GLASS AVHRR LAI product that generated from the version 4 LTDR AVHRR reflectance data. For more details we refer the reader to Xiao et al. (2017).

LAI simulated by the ORCHIDEE and VISIT models was also used to investigate the correlation between simulated GPP and LAI in process models.

2.7. Analysis methods

2.7.1. Anomaly calculation

The anomalies of GPP, meteorological, hydrological and vegetation metrics were calculated as follows:

$$X'_i = X_i - \mu \quad (2)$$

where X'_i is the anomaly of variable X in the i^{th} month or year, X_i denotes the value of variable X in the i^{th} month or year, and μ is the mean of variable X in months or years during a baseline period. Following Wolf

et al. (2016), we took the period 2008–2010 as the baseline period. After anomaly calculation, SIF and EVI data were detrended with the scipy signal library in Python.

To better present anomaly differences in space, we also calculated the spatial Z-score for flux anomalies induced by climate extremes. The Z-score was calculated as:

$$Z_i = \frac{X_i - \mu}{\sigma} \quad (3)$$

where X_i is the anomaly of variable X in the i^{th} month or year, μ and σ are the mean and standard deviation of variable X in months or years during a baseline period, respectively.

2.7.2. Correlation analysis

We used Pearson's correlation coefficient implemented in Python scipy library to quantify the correlation between simulated GPP and LAI.

3. Results

3.1. Seasonal cycle amplitude and contribution of peak growing season GPP to annual total

The two SIF-based GPP estimates (WECANN and GOPT) exhibited high agreement in seasonal cycles with peaks in July, and their seasonal cycle amplitudes (SCA) were relatively small (Fig. 1). The SCAs of the two SIF-based estimates were close to those of MOD17 and FLUXCOM. Some LUE models (VPM and CASA) and PB models (e.g. ORCHIDEE) estimated relatively large SCAs.

The mean annual totals of different GPP estimates have distinguishable differences (Fig. 1c). The two SIF-based models, FLUXCOM and MODIS GPP (MOD17) estimated lower mean annual GPP than most LUE models and PB models (Table S2). The SIF-based models ($15.55 \text{ PgC yr}^{-1}$ and $13.71 \text{ PgC yr}^{-1}$, respectively) and FLUXCOM ($15.64 \pm 1.49 \text{ PgC yr}^{-1}$) produced relatively consistent GPP estimates over North America, which is comparable to the estimate from the atmospheric inversion based on OCS ($13.97 \pm 3.59 \text{ PgC yr}^{-1}$) for the year 2010 (He and Yang, 2013). MODIS GPP was much lower than estimates of the CASA and VPM models and closer to the estimates based on the two SIF-based approaches and FLUXCOM. GPP simulated by different PB models varied largely, ranging from $14.39 \text{ PgC yr}^{-1}$ (by VEGAS) to $24.93 \text{ PgC yr}^{-1}$ (by ORCHIDEE, which estimates much larger GPP than other PB models). We further calculated the contribution of GPP_{PGS} to annual total across all models (Fig. 1d), and found the contributions reached 57.91% on the average (ranging from 40.74% by CABLE to 68.79% by VEGAS), indicating GPP_{PGS} plays an important role in determining annual total GPP.

Some LUE models (CASA and VPM) and PB models (e.g. ORCHIDEE and JULES) estimated high total GPP compared to the estimates of SIF-based approaches and FLUXCOM. Stocker et al. (2019) reported that LUE models might overestimate GPP by about 15%, owing to their exclusion of soil moisture stress on GPP, which is only indirectly accounted for through temperature factor. The overestimation or underestimation of mean annual GPP due to the deficient representation of water and temperature stresses also happen for PB models (Raczka et al., 2013). It should be kept in mind that the SIF-based estimates might suffer biases from satellite SIF data due to the uncorrected geometric angular effects (He et al., 2017b) and instrument degradation of GOME-2 (Zhang et al., 2018b).

3.2. Spatial pattern of peak growing season GPP

Following the finding that GPP_{PGS} in North America is the largest in the Corn-Belt area of Midwest US (see Fig. 2) supported by either atmospheric tracer—OCS (Hilton et al., 2017) or SIF (Guanter et al., 2014), we examined the ability of different categories of models to

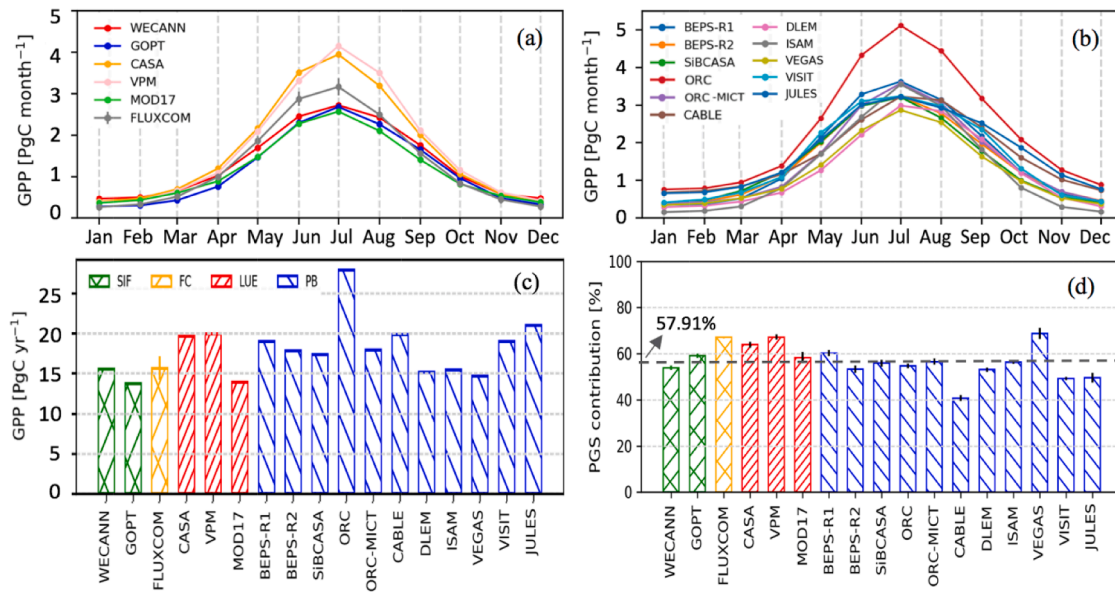


Fig. 1. Mean seasonal cycle amplitudes of GPP estimated by (a) satellite based models and FLUXCOM and (b) PB models; (c) means of annual total GPP and (d) contribution of GPP_{PGS} to annual total GPP estimated by different categories of models in North America over 2007–2014. BEPS-R1 and BEPS-R2 indicate GPP simulated by two different remotely sensed LAI products, GLOBMAP v3 and GLASS AVHRR LAI respectively.

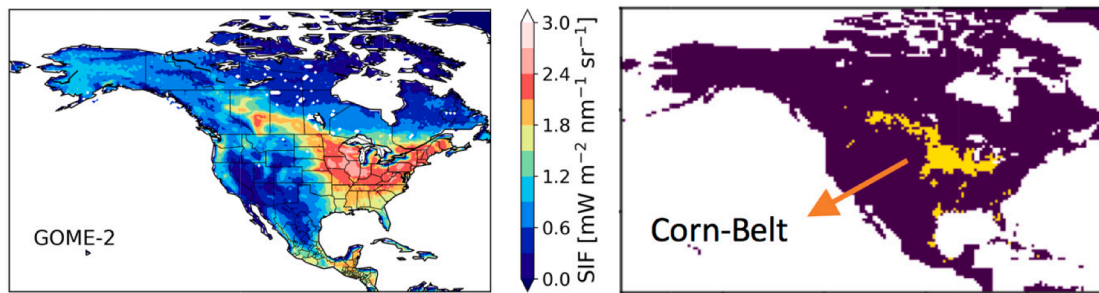


Fig. 2. (a) Mean SIF in peak growing season from GOME-2 and (b) the Corn-Belt area roughly indicated by the pattern of dense cropland in $0.5^\circ \times 0.5^\circ$ grids were presented respectively.

reproduce the spatial pattern of GPP_{PGS} (average GPP during June–August) (Fig. 3). The spatial patterns of GPP from WECANN and GOPT agreed well with each other and with the GOME-2 SIF. For interpreting SIF-based estimates, it should be kept in mind that the linear relationship between GPP and SIF varies between C3 and C4 plants and GPP is higher for C4 species with a same magnitude of SIF (Gentine and Alemohammad, 2018; Liu et al., 2017b). SIF observed by satellite sensors differs from total SIF emitted during the process of photosynthesis due to impact of canopy structure (Zhang et al., 2019b). Usually, croplands have higher escaping probability (f_{esc}) (ratio of SIF observed above the canopy to total SIF emitted), resulting in higher observed SIF. In contrast, forests have lower f_{esc} and lower SIF observed by satellites. This can explain why the higher SIF locates at the Corn-Belt area. Taking the SIF-based GPP estimates as benchmarks, we found that LUE models, especially CASA and VPM, are able to capture the spatial pattern of GPP_{PGS} quite well, higher in the Corn-Belt area. Only 3 (SiBCASA, JULES, and VEGAS) out of 10 PB models are able to reproduce spatial patterns of GPP very close to those of SIF-based GPP. ORCHIDEE, ORCHIDEE-MITC, and ISAM models performed secondly to above three PB models. Remaining PB models generally failed to reveal this pattern. Compared to SIF-based estimates, FLUXCOM estimated a larger extent of high GPP_{PGS} and MOD17 underestimated GPP in the core of the Corn-Belt area.

Fig. 4 shows the latitudinal pattern of different GPP estimates. The two SIF-based GPP estimates are almost identical. The latitudinal

patterns of FLUXCOM GPP and MOD17 GPP were close to that of SIF-based GPP. GPP of CASA and VPM was much larger than them in latitudes from $20^\circ N$ to $50^\circ N$ and from $40^\circ N$ to $60^\circ N$, respectively. The latitudinal pattern of GPP from PB models diverged largely, especially in the middle latitudinal regions. Overall, GPP estimates from PB models peaked at lower latitudes (mostly at $40^\circ N$ or lower) in comparison with those estimates from SIF-based estimates, FLUXCOM, and LUE models (mostly at $45^\circ N$).

Fig. 5 shows the comparison of GPP_{PGS} simulated by different models in the US Corn-Belt area. The mean of FLUXCOM GPP was comparable to the estimates from WECANN and GOPT. For the LUE models, MOD17 GPP was lower than WECANN GPP, GOPT GPP, and FLUXCOM GPP, while CASA GPP and VPM GPP were much higher. GPP from PB models varied in a wide range, from $0.36 \text{ PgC season}^{-1}$ (by VISIT model) to $1.04 \text{ PgC season}^{-1}$ (by ORCHIDEE model). Two PB models, VISIT and DLEM, estimated clearly lower GPP than the SIF-based and FLUXCOM GPP. On average, the PB models estimated GPP_{PGS} of the Corn-Belt area at $0.76 \pm 0.22 \text{ PgC season}^{-1}$, which is close to the SIF-based estimates ($0.76 \text{ PgC season}^{-1}$ and $0.72 \text{ PgC season}^{-1}$, respectively) and the FLUXCOM ensemble estimate ($0.79 \pm 0.10 \text{ PgC season}^{-1}$).

3.3. Response of GPP to climate extremes

Fig. 6a–b shows the comparison of the monthly anomalies of GPP estimated by the SIF-based approaches, LUE models, FLUXCOM, and PB

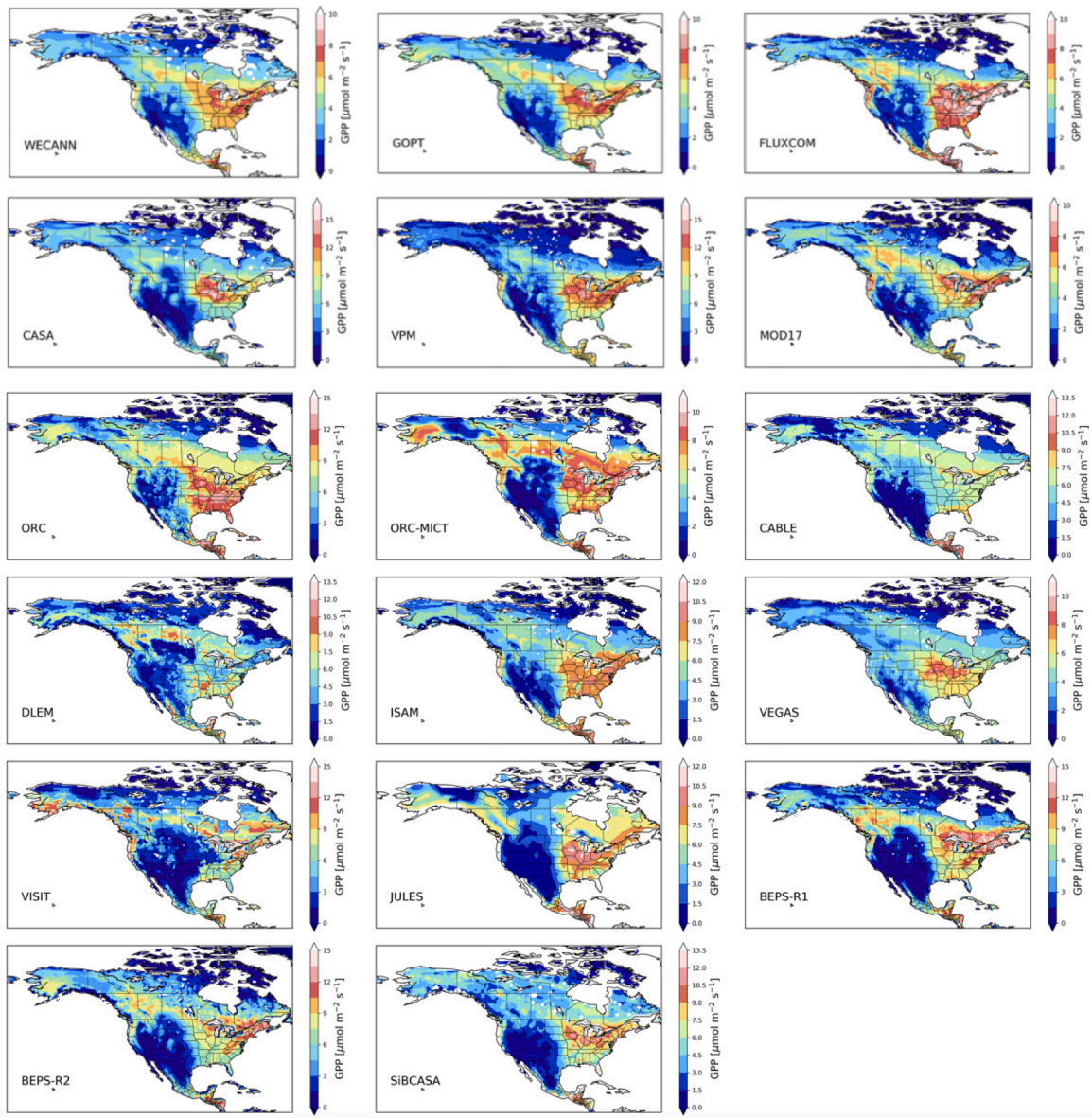


Fig. 3. Spatial patterns of mean GPP in peak growing season (June-August) simulated by different models over the period 2007–2014.

models during 2007–2014. Overall, SIF, LUE and PB models estimated consistent IAV of GPP. FLUXCOM GPP had the smaller IAV in comparison with that estimated by SIF, LUE, and PB models. The underestimation of IAV in FLUXCOM data has been reported by previous studies (He et al., 2018; Jung et al., 2020).

In the drought year 2011, noticeable discrepancies existed between the two different SIF-derived GPP data sets, implying possible uncertainties still exist in these data sets. In comparison with GOPT GPP, the monthly anomalies of WECANN GPP in 2011 were closer to those estimated by the two LUE models (CASA and VPM) and more consistent with the anomalies in EVI and SIF (Fig. 6e). These anomalies can be explained by the lower temperature in spring than normal (Fig. 6c) and lower water availability in the summer indicated by precipitation and soil moisture (Fig. 6d). The negative anomalies of GPP over the latter summer or autumn in 2011 showed in WECANN, VPM, MOD17, FLUXCOM and the ensemble mean of PB models were not well captured by GOPT and CASA. The anomalies of GPP captured by most models coincided well with those anomalies in EVI and the different SIF data sets in Fig. S1.

We also examined the physical rationale for the GPP anomalies by

comparing the retrievals and model results with climate and remotely sensed land surface variables directly. We identified several climate extremes, for example, the 2011 and 2012 drought events, with simultaneous strong reductions of precipitation, soil moisture, SIF and EVI. Discrepancies were noticeable between the anomalies of GPP estimated by SIF models and by LUE models or PB models in 2007. Both LUE and PB models showed clear negative anomalies of GPP in the latter summer or autumn, which coincided with the anomalies of SIF and EVI. SIF models showed positive anomalies of GPP. The negative anomalies of precipitation, soil moisture and EVI in late 2007 (Fig. 2) were in contrast to the positive anomaly in the SIF signal, which is likely caused by uncertainties in the SIF retrieval (see Fig. S1).

North America experienced extremely warm springs in 2010 and 2012 and severe summer droughts in 2011 and 2012. The GPP estimated by SIF (Fig. 7) and all LUE models (Fig. S2) exhibited similar anomaly responses to climate extremes. The estimated GPP increased in springs and decreased in summers of 2011 and 2012. GPP from FLUXCOM (Fig. 7) and some PB models (Fig. S3) did not respond much to these climate extremes, e.g. the 2012 warming and drought. VISIT, DLEM, and VEGAS performed relatively poor in locating GPP anomalies caused by

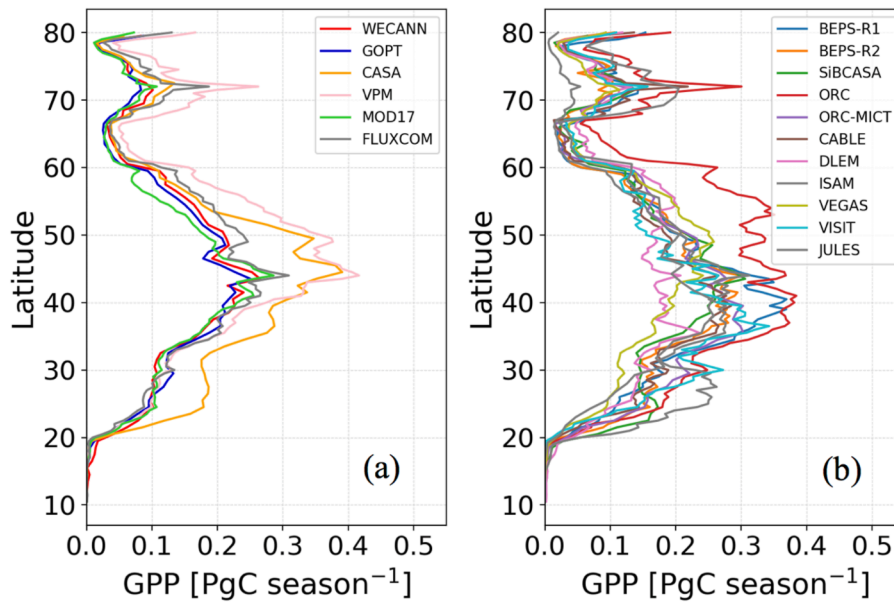


Fig. 4. Latitudinal patterns of mean GPP in the peak growing season (June-August): (a) SIF-based models, FLUXCOM, and LUE models; (b) PB models. The GPP values are summations of individual latitudes.

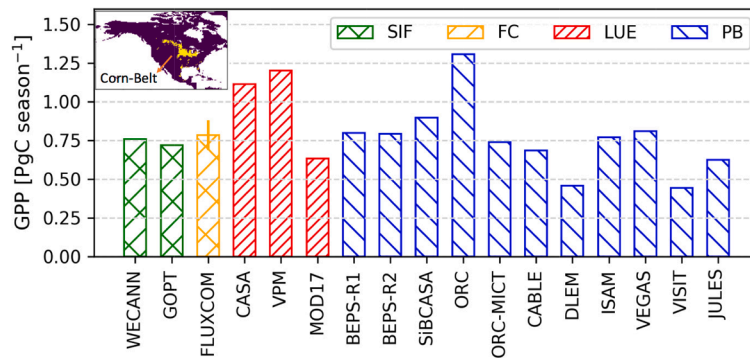


Fig. 5. Mean GPP in peak growing season (June-August) for the Corn-Belt area in North America from SIF-based estimates, FLUXCOM (short as “FC”), LUE models and PB models.

these drought events.

We further calculated the absolute GPP anomalies induced by climate extremes (Fig. 8). Overall, the satellite based models (SIF and LUE models) and most PB models clearly indicated the impact of climate extremes on North American GPP (Fig. 8), increasing in warmer springs and decreasing in the dry summers. DLEM is the exception and estimated positive GPP anomaly during the 2012 summer drought while others estimated evident negative anomalies. Among the satellite models and FLUXCOM, GOPT estimated the smallest anomalies of GPP for all four climate extreme events. CABLE estimated clearly lower GPP anomaly during the 2010 spring warming. VISIT estimated quite small anomalies of GPP for both droughts, which may attributed its distinct spatial patterns of PGS (abnormally low at the Corn-Belt area). ORCHIDEE estimated relatively large anomalies of GPP for all four climate extreme events. On average, PB models estimated larger anomalies of GPP than SIF models, FLUXCOM, and LUE models during the 2011 and 2012 summer droughts, which agrees with the previous finding that PB models generally overestimate water stress impacts on GPP (Huang et al., 2016). When looking at the standardized anomalies (Z-score; Fig. S4), the discrepancies between different models became clearly smaller.

Fig. 9 shows seasonal variations of monthly GPP anomalies in the 4 selected regions (as indicated in Fig. 7) in which the climate extreme

events occurred. The two SIF-based estimates showed large discrepancies in the magnitudes of GPP anomaly during the 2010 spring warming and the 2011 summer drought. GOPT GPP showed lower anomalies than WECANN GPP and GPP estimates from LUE models. But, it showed quite close temporal variation patterns of GPP anomalies to the ensemble mean of PB models, which may be explained by that the GOPT data assimilation relied on prior flux output from TRENDY models. At the regional scale, the difference between GOPT GPP and WECANN GPP becomes more evident. Overall, the monthly anomalies of the ensemble mean GPP of PB models exhibited relatively good consistency with those of satellite models over time during the four extreme climate events, while still diverged on the anomaly magnitudes. Noticeable differences in GPP anomalies among the SIF models, LUE models, and PB models were observed during the 2011 summer drought. Meanwhile, the PB models showed large divergence in the magnitude of estimated GPP anomalies caused by climate extreme events, typically during the 2011 drought in R3 and the 2012 drought in R4 (also see Fig. S5).

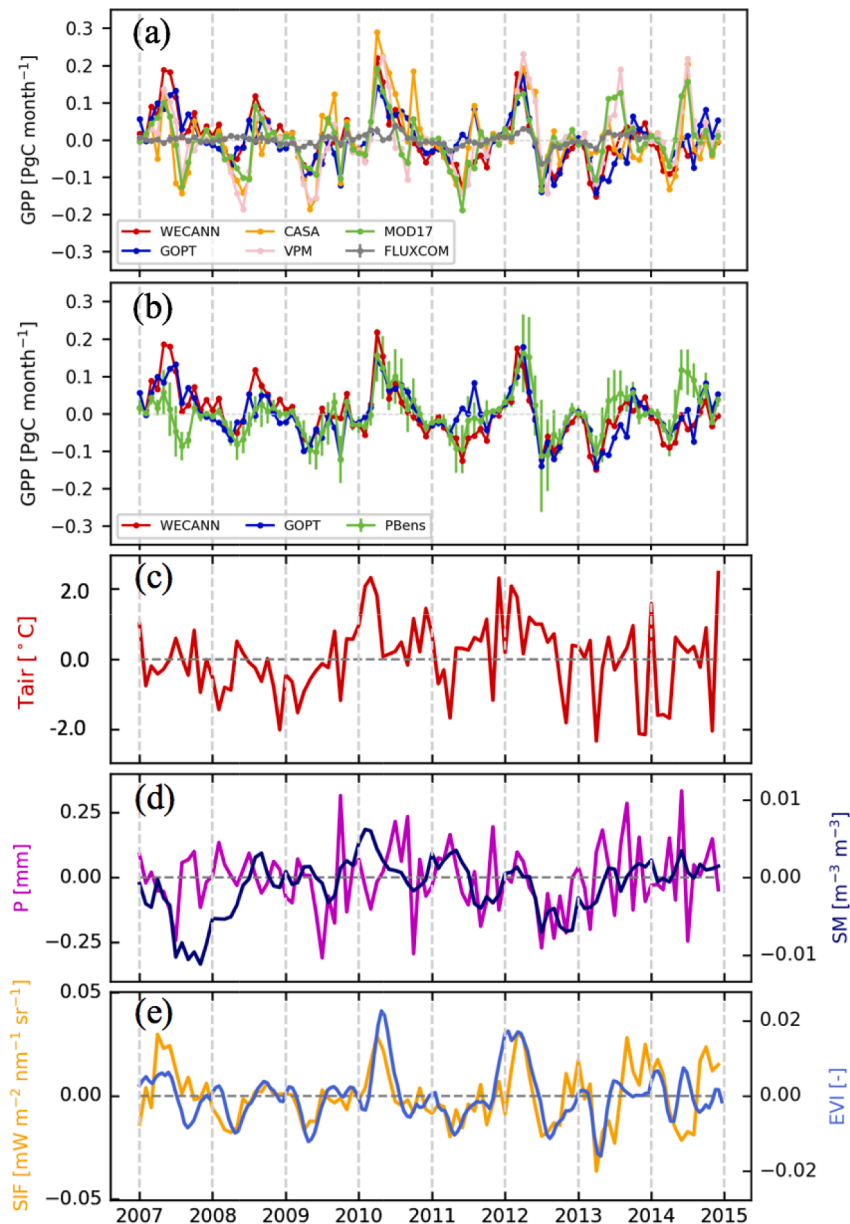


Fig. 6. (a–b) Comparisons of monthly GPP anomalies of SIF-based approaches with those of LUE models, FLUXCOM, and PB models during 2007–2014. PBens denotes the ensemble of PB models, shown with the mean values in line and the standard deviations in error bars. (c–e) Monthly anomalies of air temperature, precipitation and soil moisture, SIF and EVI during 2007–2014.

4. Discussion

4.1. Spatial pattern of peak growing season GPP in North America

GPP estimated from remotely sensed SIF (Guanter et al., 2014) and determined by atmospheric measurements of OCS (Hilton et al., 2017) indicated that the largest GPP_{PGS} within North America is located in the Corn-Belt area of Midwest U.S. We note that recent studies have identified importance of geometric angular effects on SIF (He et al., 2017a; Zhang et al., 2019b). Due to the canopy structure effect, the SIF observed by satellite sensors differs from the total SIF emitted during the process of photosynthesis.

Our study indicates that two SIF-based GPP estimates were able to replicate spatial pattern of GPP_{PGS} within North America. Differently, FLUXCOM estimated a larger extent of high GPP near the Corn-Belt area compared to the GPP estimates from SIF and LUE based modBels. It should be noted that FLUXCOM GPP relied on the trained relationship

built upon discrete in-situ GPP data from FLUXNET and MODIS data, while WECANN GPP was estimated using ANN trained with gridded GPP data from ECMWF ERA HTESSEL, FLUXNET-MTE and MODIS-GPP and GOME-2 SIF data. In principle, SIF is superior to vegetation greenness index (used in FLUXCOM algorithm) in relating to GPP across different biome types, which thus helps to produce more reliable and reasonable spatial pattern of GPP.

Likewise, LUE models (especially CASA and VPM) also reproduced the typical spatial pattern of GPP_{PGS} in the Corn-Belt area. The MOD17 model approximately mapped a reasonable spatial pattern of GPP, but MODIS GPP exhibited clear differences compared to estimates by the SIF-based and other two LUE models. Potential uncertainties of LUE models might come from fPAR (Wang et al., 2017; Zhu et al., 2016), the maximum LUE parameter (Almeida et al., 2018), and environmental controlling factors of water and temperature, and land cover classification. In term of fPAR, it is derived from either NDVI or EVI for CASA and VPM respectively, while it is estimated from LAI for the MOD17

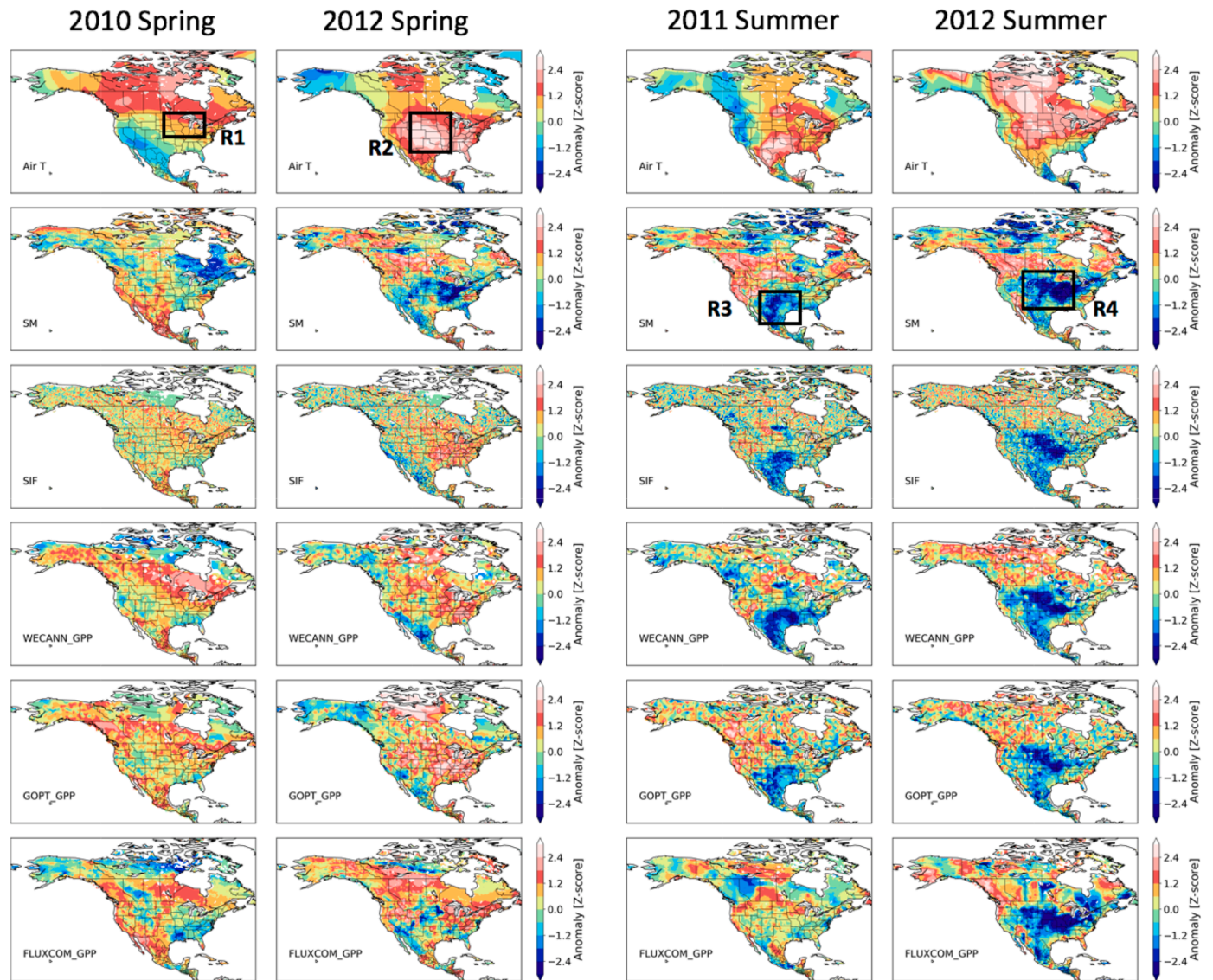


Fig. 7. Spatial pattern of the anomalies (Z-score) of air temperature, SM, SIF, and GPP in extremely spring (March to May) warmings of 2010 and 2012 and in the summer (June to August) droughts of 2011 and 2012. Four regions R1–R4 refer to the typical areas where extreme warming or drought events occurred.

model. Different from complex modeling in deriving LAI, NDVI and EVI are straightforwardly calculated from remotely sensed signals, and may suffer from less uncertainties. In addition, it is worth noting that the values of maximum LUE in CASA have been calibrated against inventory data of crop yields in U.S. (Hilton et al., 2015; Lobell et al., 2002), and CASA performed well in simulating the spatial pattern of GPP_{PGS} in North America. Also, due to the differentiation of the C3/C4 crops in LUE parametrization, the VPM model is able to capture the spatial pattern of GPP_{PGS} well (Zhang et al., 2017). On this point, SIF is effective to distinguish C3/C4 crops due to their different natures in SIF emission, which explains why SIF models characterize more reasonable spatial pattern for GPP_{PGS} .

However, except for SiBCASA, VEGAS and JULES, other PB models used here failed to capture reasonable spatial pattern of GPP_{PGS} in North America. This failure is partly attributed to their poor performances over croplands (Figs. 3 & 5), which coincides with the finding that PB models underestimate GPP in croplands by Guanter et al. (2014). The SiBCASA model outperformed the other models in mapping the spatial pattern of GPP_{PGS} , partially owing to the fact that the vegetation parameters (fPAR and LAI) are constrained by remotely sensed NDVI data. PB models generally do not represent photosynthesis well for crops (lack accurate

information on C3 and C4 and misrepresent crop as grass). In the US Corn Belt, where corn (a C4 plant) dominates, without accurate representation of crop photosynthesis in PB models resulted in their poor performance in simulating GPP_{PGS} here. As Guanter et al. (2014) suggested, cropland GPP is underestimated by PB models, yet it is possible to correct this unreasonable discrepancy by assimilating SIF information. Zhang et al. (2018a) improved cropland GPP estimate in the Corn Belt by incorporating SIF-derived spatially varying maximum carboxylation rate (V_{cmax}), which is typically assigned with a single and fixed value for each plant functional type (PFT) in PB models (Rogers, 2014; Walker et al., 2014). Another possible reason for the discrepancy could be related to LAI (also discussed in Section 4.3), as the ability to represent LAI by different models varies largely (Anav et al., 2013). We noticed the spatial pattern of GPP_{PGS} is highly correlated to prescribed or simulated LAI during PGS (Fig. S8). For most prognostic models, the simulation of LAI and assignment of V_{cmax} further depends on prescribed PFTs. Thus, the uncertainties in classification of PFTs could be another origin of uncertainties in the spatial pattern of GPP_{PGS} simulated by PB models. It is worth noting that the impacts of these structural and physical parameters on GPP_{PGS} are complex. GPP_{PGS} is usually non-linearly related to the parameterizations of specific leaf area and V_{cmax} ,

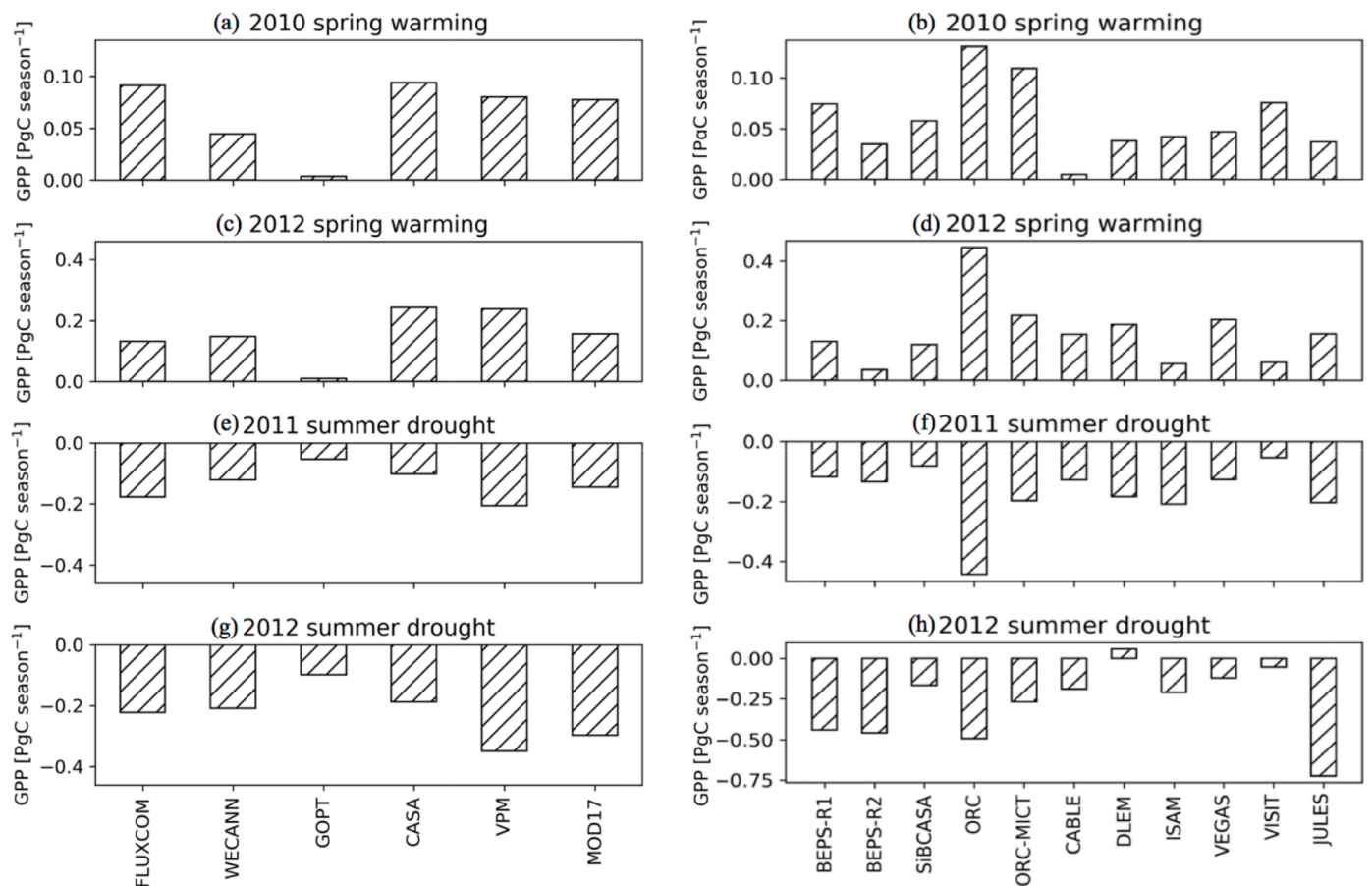


Fig. 8. Absolute anomalies of total GPP for 4 selected regions (R1~R4, indicated in Fig. 7) during the warm springs of 2010 and 2012 and the drought summers of 2011 and 2012. Subplots a,c,e and g are for FLUXCOM and remote sensing based models, and b,d,f,h are for process based models.

which could jointly control the magnitude and distribution of GPP_{PGS} (Xia et al., 2017).

The spatial pattern of estimated GPP seems not to be evidently affected by meteorological forcing data. LUE models simulated reasonable and similar spatial patterns of GPP_{PGS} although they were forced with diverse meteorological datasets. In addition, the SIBCASA model reasonably replicated the spatial pattern of GPP although it was driven by meteorological dataset different from those used by two SIF-based estimate and LUE models. The spatial patterns of GPP_{PGS} simulated by TRENDY models and the BEPS model exhibited large differences even if these models all used the same meteorological data.

4.2. Effects of water and temperature on simulated GPP

Properly simulating the IAV of carbon fluxes largely depends on the model capacity of representing effects of extremes, e.g. water and temperature stresses. The response to extremes, thus, becomes a useful means to examine model performances. From this study, we found most PB models are able to reasonably indicate IAV on the continental scale, but only few of them (ORCHIDEE, ORCHIDEE-MICT, and ISAM) are able to accurately capture responses of the carbon cycle to the 2011 and 2012 US droughts at fine scales. Most models performed poorly in indicating the spatial extent and severity of the impacts of two large-scale droughts on GPP. Recent studies revealed that state-of-the-art PB models (Kolus et al., 2019; Schewe et al., 2019) or LUE models (Stocker et al., 2019) generally underestimate drought impacts on the terrestrial carbon cycle, because current models poorly simulate the impact of water stress on GPP (Kennedy et al., 2019). Generally, PB models simulate soil water content (SWC) according to the mechanisms of water cycling in terrestrial ecosystems. However, the uncertainties of precipitation and soil

property data might induce uncertainties in simulated SWC, which have large impacts on the response of simulated GPP to droughts. Towards solving this issue, several studies attempt to improve carbon fluxes simulations under water stress (Chen et al., 2019; He et al., 2017a). A recent review offers recommendations for better representing water and temperature stresses in PB models (Rogers et al., 2017). In addition, climate extremes, for example droughts, may impact ecosystem with lagged effects. Proper simulation of lagged and accumulated effects in PB models is still challenging (Sippel et al., 2018). Most PB models performed better in capturing the response of GPP to temperature anomalies in 2010 and 2012, in comparison with their performance in simulating the impacts of droughts.

The two SIF-based estimates and three LUE models consistently captured the spatial patterns of GPP anomalies caused by either warm temperatures in springs or extreme droughts in summers. SIF is an effective indicator that sensitive to environmental stresses (Li et al., 2018; Song et al., 2018; Wang et al., 2019; Zhang et al., 2019a) and therefore SIF-based GPP responded well to climate anomalies in 2010, 2011, and 2012 over North America. Compared to the PB models, remote sensing driven LUE models have the advantage of representing the impact of environmental stresses on vegetation through the inclusion of remotely sensed variable as inputs. Taking the VPM model for example, fPAR is parameterized based on EVI, and water stress is quantified using LSWI calculated from near infrared reflectance and shortwave infrared reflectance. The latter is very sensitive to vegetation water content. EVI and LSWI contain information on the impacts of drought and temperature anomalies on terrestrial ecosystems.

Thus, our study supports further use of remote sensing data such as SIF to constrain GPP models for studying the impacts of environmental stresses on terrestrial ecosystems.

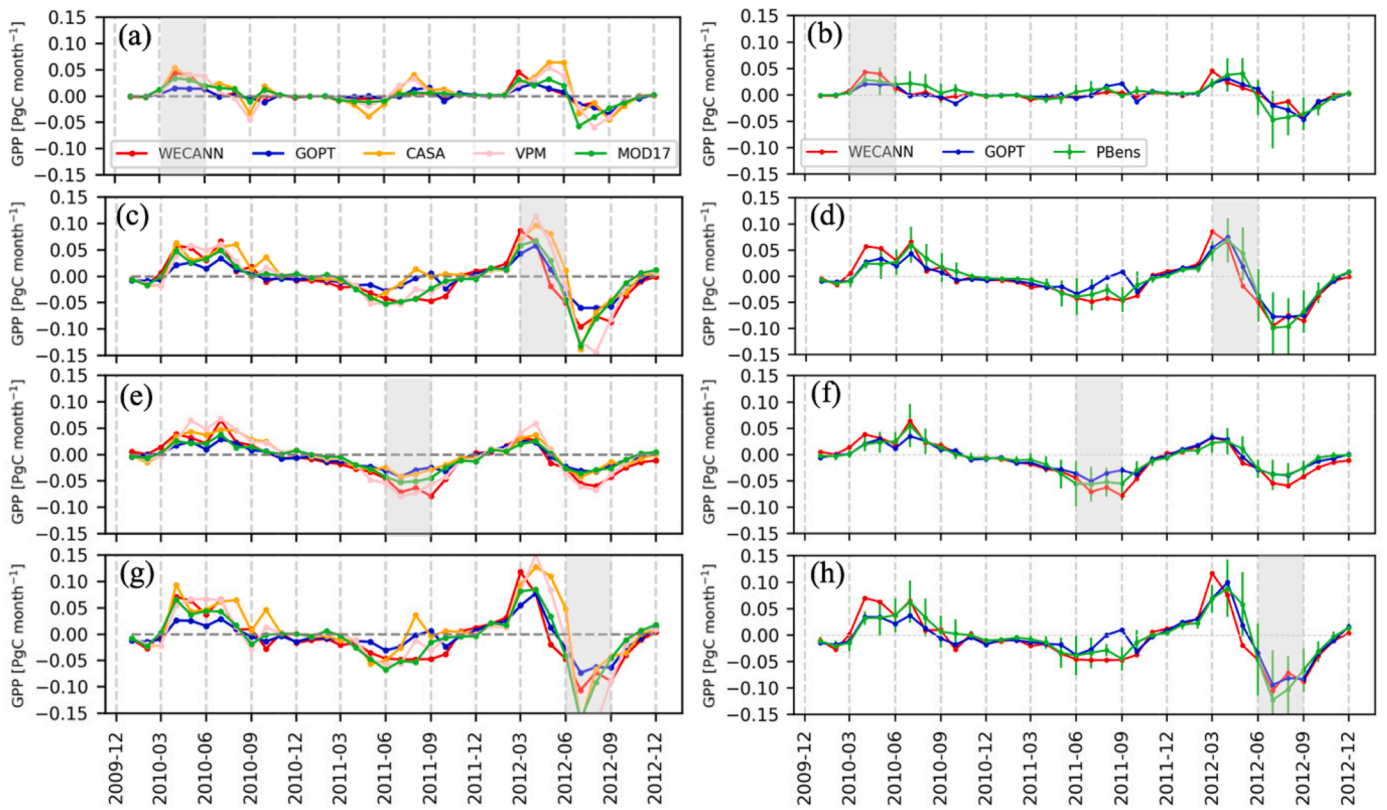


Fig. 9. Monthly GPP anomalies estimated by remote sensing models (subplots a,c,e and g) and process-based models (subplots b,d,f and h) for 4 selected regions (R1~R4, indicated in Fig. 7) during the 2010/2012 spring warmings and the 2011/2012 summer droughts. PBens denotes the ensemble of PB models, shown with the mean values in line and the standard deviations in error bars. The periods in shadow were marked as the time typical events happened in these regions.

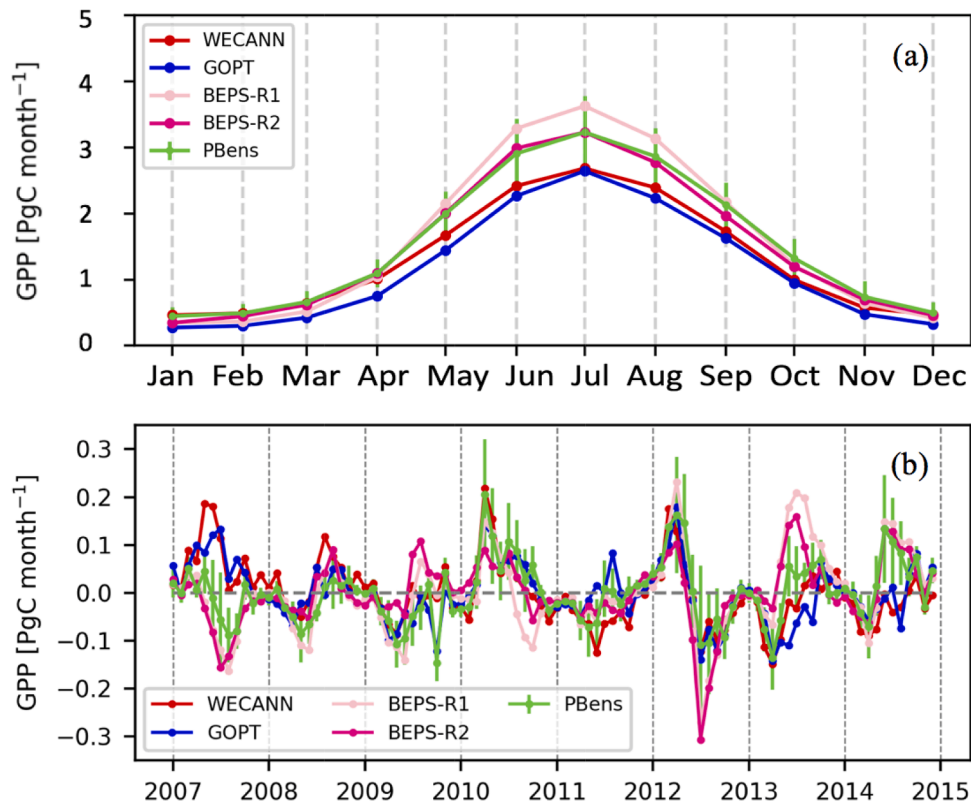


Fig. 10. The impact of LAI on seasonal cycle (a) and interannual variations (b) of simulated monthly GPP during 2007–2014. BEPS-R1 and BEPS-R2 indicate the simulated GPP driven by two different remotely sensed LAI data sets, GLOBMAP v3 and GLASS AVHRR LAI respectively.

4.3. Impact of LAI on simulated GPP by PB models

LAI is a crucial parameter for GPP simulations by PB models and uncertainty in LAI retrievals could introduce large uncertainties in the GPP estimation (Alton, 2016; Kala et al., 2014; Liu et al., 2018). From the spatial pattern of correlations between simulated GPP and LAI during PGS (Fig. S6), we found that the correlation was the strongest for the temperate region in southern North America. Based on our correlation analysis, we found that anomalies in LAI and GPP were strongly correlated over time (Fig. S7). In order to examine the impact of LAI on simulated GPP by the PB models, we performed a diagnostic experimental simulation using an alternative LAI product, the GLASS AVHRR LAI, to force the process-based BEPS model. We found the mean seasonal cycle amplitude of simulated GPP was close to the ensemble mean of the PB model simulations and the SIF-based estimates (Fig. 10a). We also noticed the simulations driven by different LAI showed noticeable difference in spatial pattern of GPP_{PGS} (Fig. S8 and Fig. 3), which confirms the impact of LAI discussed in Section 4.1. Interestingly, we found the monthly anomalies of GPP over 2007–2014 changed noticeably, e.g. in 2010 and 2013 (Fig. 10b), revealing that LAI is a critical parameter for representing the IAV of GPP in PB models. We further found the spatial patterns and the total anomalies of GPP due to climate extremes exhibited clear differences between these two simulations driven by different LAI data, e.g. during the spring warming and the summer drought in 2012 (see Fig. S3 and Fig. 8). To summarize, LAI has clear impacts on both GPP_{PGS} patterns and climate extremes-driven responses of GPP.

Moreover, the accuracy of LAI in crops and grasses largely influence GPP simulations with PB models. Testing this speculation with the CABLE (v1.4b) model, Kala et al. (2014) reported that croplands were mostly sensitive to imposed changes in LAI, with differences ranging from -90% to 60% in GPP. The plant types with high LAI and low IAV (e.g. evergreen broadleaf forests) showed the least response of simulated GPP to different LAI prescriptions, while those with lower LAI and higher IAV (e.g. croplands) were more sensitive to LAI variations. Unfortunately, LAI of crops and grasses retrieved from remote sensing data still contains considerable uncertainties (Fang et al., 2019), due to the signal saturation, background noise, intrinsic uncertainties in the radiative transfer modeling of light in canopies and the ill-posed inversion problem, and defects of retrieval methods (Fang et al., 2019; He and Yang, 2013; Shabanov et al., 2005).

Currently, despite its importance, the representation of LAI in PB models is still poor (Richardson et al., 2012). Murray-Tortarolo et al. (2013) and Anav et al. (2013) evaluated land-surface models in reproducing satellite derived LAI over the high-latitude Northern Hemisphere, and highlighted the importance to improve the ability of PB models to simulate LAI. Asaadi et al. (2018) pointed out LAI and its seasonal dynamics are key determinants of vegetation GPP and its proper simulation is crucial for PB models to capture dynamics and responses to climate change of land surface fluxes. They improved parameterization of LAI seasonality in the coupled Canadian Land Surface Scheme-Canadian Terrestrial Ecosystem Model (CLASS-CTEM, v3.6 and v2.1.1 respectively), and resulted in better agreement of simulated land surface fluxes with observations. A recent study by Lee et al. (2019) reported that the phenology model in the JULES (v4.7) model does not adequately represent the LAI for temperate forests and incorrect LAI leads to seasonal error rather than simulated yearly GPP while satellite-based LAIs are better than phenology model based LAI. The large impact of phenology on simulated GPP calls for intense research attentions.

4.4. Implications and ways to improve large-scale GPP simulations

The two SIF-based GPP estimates showed good consistency on seasonal cycle amplitude, annual total magnitude and IAV on the continental scale, as well as GPP_{PGS} spatial patterns and climate extremes-

driven responses, although they were derived with two distinct approaches (machine learning vs. data assimilation). Also, LUE models showed satisfactory performances in spatially representing GPP_{PGS} pattern and the response of the terrestrial carbon cycle to water and temperature stresses, which might be largely due to the explicit incorporation of remote sensing information. Satellite data provide unified information for all grid cells and effectively represent the sensitivities of vegetation to environmental changes. In comparison, PB models might suffer from various sources of uncertainties, stemming from defects of model structure and uncertainties in parameters and meteorological forcing. Uncertainties in prescribed plant functional types, representation of phenology (i.e. LAI), key prescribed parameters (e.g. Vcmax), the sensitivity of stomatal conductance to atmospheric and soil water deficits and high temperature would be propagated into estimated GPP (Richardson et al., 2012; Walker et al., 2017).

As indicated in our previous study (He et al., 2018), crops and grasses are dominant vegetation types in controlling the IAV of GPP in North America. A few of previous studies (Balzarolo et al., 2014; Raczka et al., 2013; Schaefer et al., 2012) also pointed out that GPP simulations from land surface models performed the poorest for cropland and grassland sites while the best for forest sites when evaluating against in-situ eddy covariance flux measurements. The divergence in IAV of GPP (Fig. 6) and spatial pattern of GPP_{PGS} (Fig. 3) over North America could be largely attributed to uncertainties in estimated GPP of crops and grasses. The improvement on simulating GPP of these two types is a prerequisite for reliable GPP estimation over this region.

Satellite observations offer new opportunity to quantify the spatio-temporal variations of key parameters regulating the functioning and carbon cycling of terrestrial ecosystems across different scales. The proper fusion of informative remotely sensed variables into PB models would help constraining uncertainties in historical GPP estimates. For example, the assimilation of remotely sensed LAI, a very important structural parameter, into PB models, was proved to evidently improve the estimated GPP at both in-situ (Ma et al., 2017) and regional (Kumar et al., 2019) scales. Recently, another important parameter, Vcmax, was successfully retrieved from satellite SIF (He et al., 2019; Zhang et al., 2014; Zhang et al., 2018a) or leaf chlorophyll content (Chl) (Alton, 2018; Houborg et al., 2013; Luo et al., 2019) and proved to improve GPP or crop yield simulations (Luo et al., 2019; Zhang et al., 2018a). Satellite SM has also been assimilated to improve GPP simulations (He et al., 2017a). Due to the close relationship between GPP and LAI, SIF, Chl or SM, assimilating these remote sensing variables into PB models (Kumar et al., 2019; Ma et al., 2017; Norton et al., 2019; Scholze et al., 2016; Wu et al., 2020) should improve their ability to characterize phenological, physiological and hydrological processes, which will be a useful way to substantially improve GPP simulations.

We are aware that most PB models are designed to conduct carbon cycle projection for the future, which means they should be fully prognostic, for example should simulate LAI, without help of real-time satellite data. But, they are also widely used to quantify historical carbon fluxes to support the assessments of global carbon budget and climate extreme impacts. The use of remotely sensed data for historical GPP simulations could help to advance our understanding of carbon cycle processes, which eventually promote the modeling of carbon cycle with PB models for future projections.

5. Conclusions

This study investigated the spatial pattern of GPP_{PGS} and responses of GPP to climate extremes over North America using a large ensemble of GPP estimates from state-of-the-art satellite and process based models. We found that two SIF-based GPP estimates (WECANN and GOPT) were bilaterally consistent in terms of spatial pattern of GPP_{PGS} (with the largest uptake at the Corn-Belt area in U.S.) and climate extremes-driven responses. The three LUE models (CASA, VPM, and MOD17) showed relatively consistent spatial pattern of GPP_{PGS} and climate extremes-

driven responses, which agreed well with SIF-based estimates and satellite based metrics. Contrastingly, the 10 PB models (including 8 TRENDY models, SiBCASA, and BEPS that driven by two different LAI data sets) exhibited noticeable divergences in spatial patterns of GPP_{P_{GS}} and most of them failed to reasonably replicate the pattern. In addition, both satellite models and PB models were comparably able to capture the impacts of climate extremes on GPP, but showing obvious divergences in the magnitude of impacts among different models. Meanwhile, satellite models generally outperformed PB models in locating GPP changes caused by climate extremes. Our study reveals the importance of satellite data, for example SIF, in improving GPP simulations especially under environmental stresses, which thus serves for accurately assessing global carbon buPCdget and impacts of climate extremes on terrestrial ecosystems.

Declaration of Competing Interest

None.

Acknowledgement

This research is funded by the National Key R&D Program of China (grant no. 2016YFA0600204). W. He is funded by the National Natural Science Foundation of China (grant no. 41907378). P. Gentine acknowledges funding from NASA NNH17ZDA001N-THP. C. Zhang is partially funded by the National Natural Science Foundation of China (grant no. 41601054). We thank ESA for providing the ESA CCI SM v3.02 soil moisture data set, Joanna Joiner for providing the GOME-2 SIF V26 data set, JPL (NASA Jet Propulsion Laboratory). We thank the Institute Pierre Simon Laplace (IPSL) of France for providing the CRUNCEP reanalysis data. A portion of this research was carried out at the Jet Propulsion Laboratory, California Institute of Technology, under contract with NASA. Support from the Earth Science Division Interdisciplinary Science (IDS) program is acknowledged. Copyright 2020. All rights reserved.

Supplementary materials

Supplementary material associated with this article can be found, in the online version, at [doi:10.1016/j.agrformet.2020.108292](https://doi.org/10.1016/j.agrformet.2020.108292).

References

- Alden, C.B., Miller, J.B., Gatti, L.V., Gloor, M.M., Guan, K., Michalak, A.M., Laan-Luijckx, I.T., Touma, D., Andrews, A., Basso, L.S., 2016. Regional atmospheric CO₂ inversion reveals seasonal and geographic differences in Amazon net biome exchange. *Global Change Biol.* 22 (10), 3427.
- Alemohammad, S.H., Fang, B., Konings, A.G., Aires, F., Green, J.K., Kolassa, J., Miralles, D., Prigent, C., Gentine, P., 2017. Water, energy, and carbon with artificial neural networks (WECANN): a statistically-based estimate of global surface turbulent fluxes and gross primary productivity using solar-induced fluorescence. *Biogeosciences* 14 (18), 4101–4124.
- Almeida, C.T.d., Delgado, R.C., Galvão, L.S., Aragão, L.E.d.O.C.e., Ramos, M.C., 2018. Improvements of the MODIS gross primary productivity model based on a comprehensive uncertainty assessment over the Brazilian Amazonia. *ISPRS J. Photogramm. Remote Sens.* 145, 268–283.
- Alton, P.B., 2016. The sensitivity of models of gross primary productivity to meteorological and leaf area forcing: A comparison between a Penman-Monteith ecophysiological approach and the MODIS Light-Use Efficiency algorithm. *Agric. For. Meteorol.* 218–219, 11–24.
- Alton, P.B., 2018. Decadal trends in photosynthetic capacity and leaf area index inferred from satellite remote sensing for global vegetation types. *Agric. For. Meteorol.* 250–251, 361–375.
- Anav, A., Murray-Tortarolo, G., Friedlingstein, P., Sitch, S., Piao, S., Zhu, Z., 2013. Evaluation of land surface models in reproducing satellite derived leaf area index over the high-latitude northern hemisphere. Part II: earth system models. *Remote Sens.* 5 (8), 3637–3661.
- Asaadi, A., Arora, V.K., Melton, J.R., Bartlett, P., 2018. An improved parameterization of leaf area index (LAI) seasonality in the Canadian Land Surface Scheme (CLASS) and Canadian Terrestrial Ecosystem Model (CTEM) modelling framework. *Biogeosciences* 15 (22), 6885–6907.
- Balzarolo, M., Boussetta, S., Balsamo, G., Beljaars, A., Maignan, F., Calvet, J.C., Lafont, S., Barbu, A., Poulter, B., Chevallier, F., Szczypta, C., Papale, D., 2014. Evaluating the potential of large-scale simulations to predict carbon fluxes of terrestrial ecosystems over a European Eddy Covariance network. *Biogeosciences* 11 (10), 2661–2678.
- Bowman, K.W., Liu, J., Bloom, A.A., Parazoo, N.C., Lee, M., Jiang, Z., Menemenlis, D., Gierach, M.M., Collatz, G.J., Gurney, K.R., Wunch, D., 2017. Global and Brazilian carbon response to El Niño Modoki 2011–2010. *Earth Space Sci.* 4 (10), 637–660.
- Byrne, B., Wunch, D., Jones, D., Strong, K., Deng, F., Baker, I., Köhler, P., Frankenberg, C., Joiner, J., Arora, V., 2018. Evaluating GPP and respiration estimates over northern midlatitude ecosystems using solar-induced fluorescence and atmospheric CO₂ measurements. *J. Geophys. Res.: Biogeosciences* 123 (9), 2976–2997.
- Chang, J., Ciaï, P., Wang, X., Piao, S., Asrar, G., Betts, R., Chevallier, F., Dury, M., François, L., Frierler, K., 2017. Benchmarking carbon fluxes of the ISIMIP2a biome models. *Environ. Res. Lett.* 12 (4), 045002.
- Chen, B., Chen, J.M., Baldocchi, D.D., Liu, Y., Wang, S., Zheng, T., Black, T.A., Croft, H., 2019. Including soil water stress in process-based ecosystem models by scaling down maximum carboxylation rate using accumulated soil water deficit. *Agric. For. Meteorol.* 276–277, 107649.
- Clark, D.B., Mercado, L.M., Sitch, S., Jones, C.D., Gedney, N., Best, M.J., Pryor, M., Rooney, G.G., Essery, R.L.H., Blyth, E., Boucher, O., Harding, R.J., Huntingford, C., Cox, P.M., 2011. The joint UK land environment simulator (JULES), model description – Part 2: carbon fluxes and vegetation dynamics. *Geosci. Model Dev.* 4 (3), 701–722.
- Dorigo, W., Wagner, W., Albergel, C., Albrecht, F., Balsamo, G., Brocca, L., Chung, D., Ertl, M., Forkel, M., Gruber, A., 2017. ESA CCI soil moisture for improved earth system understanding: state-of-the art and future directions. *Remote Sens. Environ.* 203, 185–215.
- Dorigo, W.A., Gruber, A., De Jeu, R.A.M., Wagner, W., Stacke, T., Loew, A., Albergel, C., Brocca, L., Chung, D., Parinussa, R.M., Kidd, R., 2015. Evaluation of the ESA CCI soil moisture product using ground-based observations. *Remote Sens. Environ.* 162, 380–395.
- Fang, H., Baret, F., Plummer, S., Schaepman-Strub, G., 2019. An overview of global leaf area index (LAI): methods, products, validation, and applications. *Rev. Geophys.* 57 (3), 739–799.
- Friedl, M.A., Sulla-Menashe, D., Tan, B., Schneider, A., Ramankutty, N., Sibley, A., Huang, X., 2010. MODIS collection 5 global land cover: algorithm refinements and characterization of new datasets. *Remote Sens. Environ.* 114 (1), 168–182.
- Friedlingstein, P., Cox, P., Betts, R., Bopp, L., Bloh, W.v., Brovkin, V., Cadule, P., Doney, S., Eby, M., Fung, I., Bala, G., John, J., Jones, C., Joos, F., Kato, T., Kawamiya, M., Knorr, W., Lindsay, K., Matthews, H.D., Raddatz, T., Rayner, P., Reick, C., Roeckner, E., Schnitzler, K.-G., Schnur, R., Strassmann, K., Weaver, A.J., Yoshikawa, C., Zeng, N., 2006. Climate-carbon cycle feedback analysis: results from the CAMIP model intercomparison. *J. Clim.* 19 (14), 3337–3353.
- Friedlingstein, P., Jones, M.W., O’Sullivan, M., Andrew, R.M., Hauck, J., Peters, G.P., Peters, W., Pongratz, J., Sitch, S., Le Quéré, C., Bakker, D.C.E., Canadell, J.G., Ciaï, P., Jackson, R.B., Anthoni, P., Barbero, L., Bastos, A., Bastrikov, V., Becker, M., Bopp, L., Buitenhuis, E., Chandra, N., Chevallier, F., Chini, L.P., Currie, K.I., Feely, R.A., Gehlen, M., Gilfillan, D., Gkritzalis, T., Goll, D.S., Gruber, N., Gutkunst, S., Harris, I., Havard, V., Houghton, R.A., Hurtt, G., Ilyina, T., Jain, A.K., Joetzier, E., Kaplan, J.O., Kato, E., Klein Goldewijk, K., Korsbakken, J.I., Landschützer, P., Lauvset, S.K., Lefèvre, N., Lenton, A., Lienert, S., Lombardozzi, D., Marland, G., McGuire, P.C., Melton, J.R., Metz, N., Munro, D.R., Nabel, J.E.M.S., Nakaoka, S.I., Neill, C., Omar, A.M., Ono, T., Peregón, A., Pierrot, D., Poulter, B., Rehder, G., Resplandy, L., Robertson, E., Rödenbeck, C., Séférian, R., Schwinger, J., Smith, N., Tans, P.P., Tian, H., Tilbrook, B., Tubiello, F.N., van der Werf, G.R., Wiltshire, A.J., Zaehele, S., 2019. Global carbon budget 2019. *Earth Syst. Sci. Data* 11 (4), 1783–1838.
- Gentine, P., Alemohammad, S.H., 2018. Reconstructed solar-induced fluorescence: a machine learning vegetation product based on MODIS surface reflectance to reproduce GOME-2 solar-induced fluorescence. *Geophys. Res. Lett.* 45 (7), 3136–3146.
- Guanter, L., Zhang, Y., Jung, M., Joiner, J., Voigt, M., Berry, J.A., Frankenberg, C., Huete, A.R., Zarco-Tejada, P., Lee, J.E., 2014. Global and time-resolved monitoring of crop photosynthesis with chlorophyll fluorescence. In: *Proceedings of the National Academy of Sciences of the United States of America*, 111, pp. 1327–1333.
- Guimberteau, M., Zhu, D., Maignan, F., Huang, Y., Yue, C., Dantec-Nédélec, S., Otlé, C., Jorret-Puig, A., Bastos, A., Laurent, P., Goll, D., Bowring, S., Chang, J., Guenet, B., Tifafi, M., Peng, S., Krinner, G., Ducharne, A., Wang, F., Wang, T., Wang, X., Wang, Y., Yin, Z., Lauerwald, R., Joetzier, E., Qiu, C., Kim, H., Ciaï, P., 2018. ORCHIDEE-MICT (v8.4.1), a land surface model for the high latitudes: model description and validation. *Geosci. Model Dev.* 11 (1), 121–163.
- He, L., Chen, J.M., Liu, J., Bélair, S., Luo, X., 2017a. Assessment of SMAP soil moisture for global simulation of gross primary production. *J. Geophys. Res.: Biogeosciences* 122 (7), 1549–1563.
- He, L., Chen, J.M., Liu, J., Mo, G., Joiner, J., 2017b. Angular normalization of GOME-2 Sun-induced chlorophyll fluorescence observation as a better proxy of vegetation productivity. *Geophys. Res. Lett.* 44 (11), 5691–5699.
- He, L., Chen, J.M., Liu, J., Zheng, T., Wang, R., Joiner, J., Chou, S., Chen, B., Liu, Y., Liu, R., Rogers, C., 2019. Diverse photosynthetic capacity of global ecosystems mapped by satellite chlorophyll fluorescence measurements. *Remote Sens. Environ.* 232, 111344.
- He, W., Ju, W., Schwalm, C.R., Sippel, S., Wu, X., He, Q., Song, L., Zhang, C., Li, J., Sitch, S., 2018. Large-scale droughts responsible for dramatic reductions of terrestrial net carbon uptake over North America in 2011 and 2012. *J. Geophys. Res.: Biogeosciences* 123 (7), 2053–2071.

- He, W., Yang, H., 2013. Winter wheat leaf area index retrieval with multi-angle and multi-spectral Terra/Aqua MODIS data. *Trans. Chin. Soc. Agric. Eng.* 29 (4), 2053–2071.
- Hilton, T.W., Whelan, M.E., Zumkehr, A., Kulkarni, S., Berry, J.A., Baker, I.T., Montzka, S.A., Sweeney, C., Miller, B.R., Campbell, J.E., 2017. Peak growing season gross uptake of carbon in North America is largest in the Midwest USA. *Nat. Clim. Change* 7 (6), 450–454.
- Hilton, T.W., Zumkehr, A., Kulkarni, S., Berry, J., Whelan, M.E., Campbell, J.E., 2015. Large variability in ecosystem models explains uncertainty in a critical parameter for quantifying GPP with carbonyl sulphide. *Tellus B* 67.
- Houborg, R., Cescatti, A., Migliavacca, M., Kustas, W.P., 2013. Satellite retrievals of leaf chlorophyll and photosynthetic capacity for improved modeling of GPP. *Agric. For. Meteorol.* 177, 10–23.
- Huang, K., Xia, J., Wang, Y., Ahlström, A., Chen, J., Cook, R.B., Cui, E., Fang, Y., Fisher, J.B., Huntzinger, D.N., Li, Z., Michalak, A.M., Qiao, Y., Schaefer, K., Schwalm, C., Wang, J., Wei, Y., Xu, X., Yan, L., Bian, C., Luo, Y., 2018. Enhanced peak growth of global vegetation and its key mechanisms. *Nat. Ecol. Evol.* 2 (12), 1897–1905.
- Huang, Y., Gerber, S., Huang, T., Lichstein, J.W., 2016. Evaluating the drought response of CMIP5 models using global gross primary productivity, leaf area, precipitation and soil moisture data. *Glob. Biogeochem. Cycles* 30 (12), 1827–1846.
- Huete, A., Didan, K., Miura, T., Rodriguez, E.P., Gao, X., Ferreira, L.G., 2002. Overview of the radiometric and biophysical performance of the MODIS vegetation indices. *Remote Sens. Environ.* 83 (1), 195–213.
- Huntzinger, D.N., Michalak, A., Schwalm, C., Ciais, P., King, A., Fang, Y., Schaefer, K., Wei, Y., Cook, R., Fisher, J., 2017. Uncertainty in the response of terrestrial carbon sink to environmental drivers undermines carbon-climate feedback predictions. *Sci. Rep.* 7 (1), 4765.
- Huntzinger, D.N., Post, W.M., Wei, Y., Michalak, A., West, T.O., Jacobson, A., Baker, I., Chen, J.M., Davis, K., Hayes, D., 2012. North American carbon program (NACP) regional interim synthesis: terrestrial biospheric model intercomparison. *Ecol. Modell.* 232, 144–157.
- Ito, A., Inatomi, M., Huntzinger, D.N., Schwalm, C., Michalak, A.M., Cook, R., King, A., Mao, J., Wei, Y., Mac Post, W., 2016. Decadal trends in the seasonal-cycle amplitude of terrestrial CO₂ exchange resulting from the ensemble of terrestrial biosphere models. *Tellus B* 68, 28968.
- Ito, A., Nishina, K., Reyer, C.P., François, L., Henrot, A.-J., Munhoven, G., Jacquemin, I., Tian, H., Yang, J., Pan, S., 2017. Photosynthetic productivity and its efficiencies in ISMIP2a biome models: benchmarking for impact assessment studies. *Environ. Res. Lett.* 12 (8), 085001.
- Jain, A.K., Meiyappan, P., Song, Y., House, J.I., 2013. CO₂ emissions from land-use change affected more by nitrogen cycle, than by the choice of land-cover data. *Global Change Biol.* 19 (9), 2893–2906.
- Joiner, J., Guanter, L., Lindstrot, R., Voigt, M., Vasilkov, A.P., Middleton, E.M., Huemrich, K.F., Yoshida, Y., Frankenberg, C., 2013. Global monitoring of terrestrial chlorophyll fluorescence from moderate-spectral-resolution near-infrared satellite measurements: methodology, simulations, and application to GOME-2. *Atmos. Meas. Tech.* 6 (10), 2803–2823.
- Joiner, J., Yoshida, Y., Vasilkov, A.P., Yoshida, Y., Corp, L.A., Middleton, E.M., 2011. First observations of global and seasonal terrestrial chlorophyll fluorescence from space. *Biogeosciences* 8 (3), 637–651.
- Jönsson, P., Eklundh, L., 2004. TIMESAT—a program for analyzing time-series of satellite sensor data. *Comput. Geosci.* 30 (8), 833–845.
- Ju, W., Chen, J.M., Black, T.A., Barr, A.G., Liu, J., Chen, B., 2006. Modelling multi-year coupled carbon and water fluxes in a boreal aspen forest. *Agric. For. Meteorol.* 140 (1), 136–151.
- Jung, M., Reichstein, M., Schwalm, C.R., Huntingford, C., Sitch, S., Ahlström, A., Arneth, A., Camps-Valls, G., Ciais, P., Friedlingstein, P., Gans, F., Ichii, K., Jain, A.K., Kato, E., Papale, D., Poulter, B., Raduly, B., Rödenbeck, C., Tramontana, G., Viovy, N., Wang, Y.-P., Weber, U., Zaehle, S., Zeng, N., 2017. Compensatory water effects link yearly global land CO₂ sink changes to temperature. *Nature* 541 (7638), 516–520.
- Kala, J., Decker, M., Exbrayat, J.-F., Pitman, A.J., Carouge, C., Evans, J.P., Abramowitz, G., Mocko, D., 2014. Influence of leaf area index prescriptions on simulations of heat, moisture, and carbon fluxes. *J. Hydrometeorol.* 15 (1), 489–503.
- Kato, E., Kinoshita, T., Ito, A., Kawamiya, M., Yamagata, Y., 2013. Evaluation of spatially explicit emission scenario of land-use change and biomass burning using a process-based biogeochemical model. *J. Land Use Sci.* 8 (1), 104–122.
- Kennedy, D., Swenson, S., Oleson, K.W., Lawrence, D.M., Fisher, R., Lola da Costa, A.C., Gentile, P., 2019. Implementing plant hydraulics in the community land model, version 5. *J. Adv. Model. Earth Syst.* 11 (2), 485–513.
- Kolus, H.R., Huntzinger, D.N., Schwalm, C.R., Fisher, J.B., McKay, N., Fang, Y., Michalak, A.M., Schaefer, K., Wei, Y., Poulter, B., Mao, J., Parazoo, N.C., Shi, X., 2019. Land carbon models underestimate the severity and duration of drought's impact on plant productivity. *Sci. Rep.* 9 (1), 2758.
- Krinner, G., Viovy, N., de Noblet-Ducoudré, N., Ogée, J., Polcher, J., Friedlingstein, P., Ciais, P., Sitch, S., Prentice, I.C., 2005. A dynamic global vegetation model for studies of the coupled atmosphere-biosphere system. *Glob. Biogeochem. Cycles* 19 (1).
- Kumar, S.V., Mocko, M., D., Wang, S., Peters-Lidard, C.D., Borak, J., 2019. Assimilation of remotely sensed leaf area index into the Noah-MP land surface model: impacts on water and carbon fluxes and states over the continental United States. *J. Hydrometeorol.* 20 (7), 1359–1377.
- Lasslop, G., Reichstein, M., Papale, D., Richardson, A.D., Arneth, A., Barr, A., Stoy, P., Wohlfahrt, G., 2010. Separation of net ecosystem exchange into assimilation and respiration using a light response curve approach: critical issues and global evaluation. *Global Change Biol.* 16 (1), 187–208.
- Lee, H., Park, J., Cho, S., Lee, M., Kim, H.S., 2019. Impact of leaf area index from various sources on estimating gross primary production in temperate forests using the JULES land surface model. *Agric. For. Meteorol.* 276–277, 107614.
- Lee, J.-E., Frankenberg, C., van der Tol, C., Berry, J.A., Guanter, L., Boyce, C.K., Fisher, J. B., Morrow, E., Worden, J.R., Asefi, S., 2013. Forest productivity and water stress in Amazonia: observations from GOSAT chlorophyll fluorescence. *Proc. R. Soc. Lond. B: Biol. Sci.* 280 (1761), 20130171.
- Li, X., Li, Y., Chen, A., Gao, M., Slette, L.J., Piao, S., 2019. The impact of the 2009/2010 drought on vegetation growth and terrestrial carbon balance in Southwest China. *Agric. For. Meteorol.* 269–270, 239–248.
- Li, X., Xiao, J., He, B., 2018. Higher absorbed solar radiation partly offset the negative effects of water stress on the photosynthesis of Amazon forests during the 2015 drought. *Environ. Res. Lett.* 13 (4), 044005.
- Li, Y., Yang, H., Wang, T., MacBean, N., Bacour, C., Ciais, P., Zhang, Y., Zhou, G., Piao, S., 2017. Reducing the uncertainty of parameters controlling seasonal carbon and water fluxes in Chinese forests and its implication for simulated climate sensitivities. *Glob. Biogeochem. Cycles* 31 (8), 1344–1366.
- Liu, J., Bowman, K.W., Schimel, D.S., Parazoo, N.C., Jiang, Z., Lee, M., Bloom, A.A., Wunch, D., Frankenberg, C., Sun, Y., 2017a. Contrasting carbon cycle responses of the tropical continents to the 2015–2016 El Niño. *Science* 358 (6360), eaam5690.
- Liu, J., Chen, J.M., Cihlar, J., Park, W.M., 1997. A process-based boreal ecosystem productivity simulator using remote sensing inputs. *Remote Sens. Environ.* 62 (2), 158–175.
- Liu, L., Guan, L., Liu, X., 2017b. Directly estimating diurnal changes in GPP for C3 and C4 crops using far-red sun-induced chlorophyll fluorescence. *Agric. For. Meteorol.* 232, 1–9.
- Liu, Y., Liu, R., Chen, J.M., 2012. Retrospective retrieval of long-term consistent global leaf area index (1981–2011) from combined AVHRR and MODIS data. *J. Geophys. Res.: Biogeosciences* 117 (G4).
- Liu, Y., Xiao, J., Ju, W., Zhu, G., Wu, X., Fan, W., Li, D., Zhou, Y., 2018. Satellite-derived LAI products exhibit large discrepancies and can lead to substantial uncertainty in simulated carbon and water fluxes. *Remote Sensing of Environment* 206, 174–188.
- Lobell, D.B., Hicke, J.A., Asner, G.P., Field, C.B., Tucker, C.J., Los, S.O., 2002. Satellite estimates of productivity and light use efficiency in United States agriculture, 1982–98. *Global Change Biol.* 8 (8), 722–735.
- Luo, X., Croft, H., Chen, J.M., He, L., Keenan, T.F., 2019. Improved estimates of global terrestrial photosynthesis using information on leaf chlorophyll content. *Global Change Biol.* 25 (7), 2499–2514.
- Ma, R., Zhang, L., Tian, X., Zhang, J., Yuan, W., Zheng, Y., Zhao, X., Kato, T., 2017. Assimilation of remotely-sensed leaf area index into a dynamic vegetation model for gross primary productivity estimation. *Remote Sens.* 9 (3), 188.
- MacBean, N., Maignan, F., Bacour, C., Lewis, P., Peylin, P., Guanter, L., Köhler, P., Gómez-Dans, J., Disney, M., 2018. Strong constraint on modelled global carbon uptake using solar-induced chlorophyll fluorescence data. *Sci. Rep.* 8 (1), 1973.
- Martens, B., Gonzalez Miralles, D., Lievens, H., van der Schalie, R., de Jeu, R.A., Fernández-Prieto, D., Beck, H.E., Dorigo, W., Verhoest, N., 2017. GLEAM v3: Satellite-based land evaporation and root-zone soil moisture. *Geosci. Model Dev.* 10 (5), 1903–1925.
- Miralles, D.G., Holmes, T.R.H., De Jeu, R.A.M., Gash, J.H., Meesters, A.G.C.A., Dolman, A.J., 2011. Global land-surface evaporation estimated from satellite-based observations. *Hydrol. Earth Syst. Sci.* 15 (2), 453–469.
- Monteith, J., 1972. Solar radiation and productivity in tropical ecosystems. *J. Appl. Ecol.* 9 (3), 747–766.
- Monteith, J.L., 1977. Climate and the efficiency of crop production in Britain. *Philos. Trans. R. Soc. Lond. B, Biol. Sci.* 281 (980), 277–294.
- Murray-Tortarolo, G., Anav, A., Friedlingstein, P., Sitch, S., Piao, S., Zhu, Z., Poulter, B., Zaehle, S., Ahlström, A., Lomas, M., Levis, S., Viovy, N., Zeng, N., 2013. Evaluation of land surface models in reproducing satellite-derived LAI over the high-latitude northern hemisphere. Part I: uncoupled DGVMs. *Remote Sens.* 5 (10), 4819–4838.
- New, M., Hulme, M., Jones, P., 2000. Representing twentieth-century space-time climate variability. Part II: development of 1901–96 monthly grids of terrestrial surface climate. *J. Clim.* 13 (13), 2217–2238.
- Norton, A.J., Rayner, P.J., Koffi, E.N., Scholze, M., Silver, J.D., Wang, Y.P., 2019. Estimating global gross primary productivity using chlorophyll fluorescence and a data assimilation system with the BETHY-SCOPE model. *Biogeosciences* 16 (15), 3069–3093.
- Parazoo, N.C., Barnes, E., Worden, J., Harper, A.B., Bowman, K.B., Frankenberg, C., Wolf, S., Litvak, M., Keenan, T.F., 2015. Influence of ENSO and the NAO on terrestrial carbon uptake in the Texas-northern Mexico region. *Glob. Biogeochem. Cycles* 29 (8), 1247–1265.
- Parazoo, N.C., Bowman, K., Fisher, J.B., Frankenberg, C., Jones, D., Cescatti, A., Pérez-Priego, Ó., Wohlfahrt, G., Montagnani, L., 2014. Terrestrial gross primary production inferred from satellite fluorescence and vegetation models. *Global Change Biol.* 20 (10), 3103–3121.
- Peng, J., Niesel, J., Loew, A., Zhang, S., Wang, J., 2015. Evaluation of satellite and reanalysis soil moisture products over Southwest China using ground-based measurements. *Remote Sens.* 7 (11), 15729–15747.
- Potter, C.S., Randerson, J.T., Field, C.B., Matson, P.A., Vitousek, P.M., Mooney, H.A., Klooster, S.A., 1993. Terrestrial ecosystem production: a process model based on global satellite and surface data. *Glob. Biogeochem. Cycles* 7 (4), 811–841.
- Raczka, B.M., Davis, K.J., Huntzinger, D., Neilson, R.P., Poulter, B., Richardson, A.D., Xiao, J., Baker, I., Ciais, P., Keenan, T.F., Law, B., Post, W.M., Ricciuto, D., Schaefer, K., Tian, H., Tomelleri, E., Verbeeck, H., Viovy, N., 2013. Evaluation of

- continental carbon cycle simulations with North American flux tower observations. *Ecol. Monographs* 83 (4), 531–556.
- Randerson, J.T., Thompson, M.V., Malmstrom, C.M., Field, C.B., Fung, I.Y., 1996. Substrate limitations for heterotrophs: implications for models that estimate the seasonal cycle of atmospheric CO₂. *Glob. Biogeochem. Cycles* 10 (4), 585–602.
- Reichstein, M., Bahn, M., Mahecha, M.D., Kattge, J., Baldocchi, D.D., 2014. Linking plant and ecosystem functional biogeography. *Proc. Natl. Acad. Sci.* 111 (38), 13697–13702.
- Reichstein, M., Falge, E., Baldocchi, D., Papale, D., Aubinet, M., Berbigier, P., Bernhofer, C., Buchmann, N., Gilmanov, T., Granier, A., Grünwald, T., Havránková, K., Ilvesniemi, H., Janous, D., Knohl, A., Laurila, T., Lohila, A., Loustau, D., Matteucci, G., Meyers, T., Miglietta, F., Ourcival, J.-M., Pumpanen, J., Rambal, S., Rotenberg, E., Sanz, M., Tenhunen, J., Seufert, G., Vaccari, F., Vesala, T., Yakir, D., Valentini, R., 2005. On the separation of net ecosystem exchange into assimilation and ecosystem respiration: review and improved algorithm. *Global Change Biol.* 11 (9), 1424–1439.
- Richardson, A.D., Anderson, R.S., Arain, M.A., Barr, A.G., Bohrer, G., Chen, G., Chen, J. M., Ciais, P., Davis, K.J., Desai, A.R., Dietze, M.C., Dragoni, D., Garrity, S.R., Gough, C.M., Grant, R., Hollinger, D.Y., Margolis, H.A., McCaughey, H., Migliavacca, M., Monson, R.K., Munger, J.W., Poulter, B., Raczka, B.M., Ricciuto, D. M., Sahoo, A.K., Schaefer, K., Tian, H., Vargas, R., Verbeeck, H., Xiao, J., Xue, Y., 2012. Terrestrial biosphere models need better representation of vegetation phenology: results from the North American Carbon Program Site Synthesis. *Global Change Biol.* 18 (2), 566–584.
- Rienecker, M.M., Suarez, M.J., Gelaro, R., Todling, R., Bacmeister, J., Liu, E., Bosilovich, M.G., Schubert, S.D., Takacs, L., Kim, G.-K., Bloom, S., Chen, J., Collins, D., Conaty, A., da Silva, A., Gu, W., Joiner, J., Koster, R.D., Lucchesi, R., Molod, A., Owens, T., Pawson, S., Pegion, P., Redder, C.R., Reichle, R., Robertson, F. R., Ruddick, A.G., Sienkiewicz, M., Woollen, J., 2011. MERRA: NASA's modern-era retrospective analysis for research and applications. *J. Clim.* 24 (14), 3624–3648.
- Rogers, A., 2014. The use and misuse of Vc,max in Earth System Models. *Photosynth. Res.* 119 (1), 15–29.
- Rogers, A., Medlyn, B.E., Dukes, J.S., Bonan, G., Von Caemmerer, S., Dietze, M.C., Kattge, J., Leakey, A.D., Mercado, L.M., Niinemets, Ü., 2017. A roadmap for improving the representation of photosynthesis in Earth system models. *New Phytol.* 213 (1), 22–42.
- Running, S.W., Nemani, R.R., Heinsch, F.A., Zhao, M., Reeves, M., Hashimoto, H., 2004. A continuous satellite-derived measure of global terrestrial primary production. *Bioscience* 54 (6), 547–560.
- Running, S.W., Zhao, M., 2015. Daily GPP and annual NPP (MOD17A2/A3) products NASA Earth Observing System MODIS land algorithm. MOD17 User's Guide, 2015.
- Schaefer, K., Collatz, G.J., Tans, P., Denning, A.S., Baker, I., Berry, J., Prihodko, L., Suits, N., Philpott, A., 2008. Combined simple biosphere/Carnegie-Ames-Stanford approach terrestrial carbon cycle model. *J. Geophys. Res.: Biogeosciences* 113 (G3).
- Schaefer, K., Schwalm, C.R., Williams, C., Arain, M.A., Barr, A., Chen, J.M., Davis, K.J., Dimitrov, D., Hilton, T.W., Hollinger, D.Y., Humphreys, E., Poulter, B., Raczka, B.M., Richardson, A.D., Sahoo, A., Thornton, P., Vargas, R., Verbeeck, H., Anderson, R., Baker, I., Black, T.A., Bolstad, P., Chen, J., Curtis, P.S., Desai, A.R., Dietze, M., Dragoni, D., Gough, C., Grant, R.F., Gu, L., Jain, A., Kucharik, C., Law, B., Liu, S., Lokipitaya, E., Margolis, H.A., Matamala, R., McCaughey, J.H., Monson, R., Munger, J.W., Oechel, W., Peng, C., Price, D.T., Ricciuto, D., Riley, W.J., Roulet, N., Tian, H., Tonitto, C., Torn, M., Weng, E., Zhou, X., 2012. A model-data comparison of gross primary productivity: results from the North American carbon program site synthesis. *J. Geophys. Res.: Biogeosciences* 117 (G3).
- Schewe, J., Gosling, S.N., Reyer, C., Zhao, F., Ciais, P., Elliott, J., Francois, L., Huber, V., Lotze, H.K., Seneviratne, S.I., 2019. State-of-the-art global models underestimate impacts from climate extremes. *Nat. Commun.* 10 (1), 1005.
- Scholze, M., Kaminski, T., Knorr, W., Blessing, S., Vossbeck, M., Grant, J.P., Scipal, K., 2016. Simultaneous assimilation of SMOS soil moisture and atmospheric CO₂ in-situ observations to constrain the global terrestrial carbon cycle. *Remote Sens. Environ.* 180, 334–345.
- Shabanov, N.V., Dong, H., Wenze, Y., Tan, B., Knyazikhin, Y., Myneni, R.B., Ahl, D.E., Gower, S.T., Huete, A.R., Aragao, L.E.O.C., Shimabukuro, Y.E., 2005. Analysis and optimization of the MODIS leaf area index algorithm retrievals over broadleaf forests. *IEEE Trans. Geosci. Remote Sens.* 43 (8), 1855–1865.
- Sippel, S., Reichstein, M., Ma, X., Mahecha, M.D., Lange, H., Flach, M., Frank, D., 2018. Drought, heat, and the carbon cycle: a review. *Curr. Clim. Change Rep.* 4 (3), 266–286.
- Sitch, S., Friedlingstein, P., Gruber, N., Jones, S., Murray-Tortarolo, G., Ahlström, A., Doney, S.C., Graven, H., Heinze, C., Huntingford, C., 2015. Recent trends and drivers of regional sources and sinks of carbon dioxide. *Biogeosciences* 12 (3), 653–679.
- Slevin, D., Tett, S.F., Exbrayat, J.-F., Bloom, A.A., Williams, M., 2017. Global evaluation of gross primary productivity in the JULES land surface model v3. 4.1. *Geosci. Model Dev.* 10 (7), 2651–2670.
- Song, L., Guanter, L., Guan, K., You, L., Huete, A., Ju, W., Zhang, Y., 2018. Satellite sun-induced chlorophyll fluorescence detects early response of winter wheat to heat stress in the Indian Indo-Gangetic Plains. *Global Change Biol.* 24 (9), 4023–4037.
- Stocker, B.D., Zscheischler, J., Keenan, T.F., Prentice, I.C., Seneviratne, S.I., Peñuelas, J., 2019. Drought impacts on terrestrial primary production underestimated by satellite monitoring. *Nat. Geosci.* 12 (4), 264–270.
- Sun, Y., Fu, R., Dickinson, R., Joiner, J., Frankenberg, C., Gu, L., Xia, Y., Fernando, N., 2015. Drought onset mechanisms revealed by satellite solar-induced chlorophyll fluorescence: Insights from two contrasting extreme events. *J. Geophys. Res.: Biogeosciences* 120 (11), 2427–2440.
- Tian, H., Chen, G., Lu, C., Xu, X., Hayes, D.J., Ren, W., Pan, S., Huntzinger, D.N., Wofsy, S.C., 2015. North American terrestrial CO₂ uptake largely offset by CH₄ and N₂O emissions: toward a full accounting of the greenhouse gas budget. *Clim. Change* 129 (3–4), 413–426.
- Tramontana, G., Jung, M., Schwalm, C.R., Ichii, K., Camps-Valls, G., Ráduly, B., Reichstein, M., Arain, M.A., Cescatti, A., Kiely, G., Merbold, L., Serrano-Ortiz, P., Sickert, S., Wolf, S., Papale, D., 2016. Predicting carbon dioxide and energy fluxes across global FLUXNET sites with regression algorithms. *Biogeosciences* 13 (14), 4291–4313.
- van der Velde, I., Miller, J., Schaefer, K., van der Werf, G., Krol, M., Peters, W., 2014. Terrestrial cycling of ¹³CO₂ by photosynthesis, respiration, and biomass burning in SiBCASA. *Biogeosciences* 11, 6553–6571.
- Van der Werf, G.R., Randerson, J.T., Giglio, L., Collatz, G., Mu, M., Kasibhatla, P.S., Morton, D.C., DeFries, R., Jin, Y.v., van Leeuwen, T.T., 2010. Global fire emissions and the contribution of deforestation, savanna, forest, agricultural, and peat fires (1997–2009). *Atmos. Chem. Phys.* 10 (23), 11707–11735.
- Walker, A.P., Beckerman, A.P., Gu, L., Kattge, J., Cernusak, L.A., Domingues, T.F., Scales, J.C., Wohlfahrt, G., Wullschlegel, S.D., Woodward, F.I., 2014. The relationship of leaf photosynthetic traits – Vc,max and Jmax – to leaf nitrogen, leaf phosphorus, and specific leaf area: a meta-analysis and modeling study. *Ecol. Evol.* 4 (16), 3218–3235.
- Walker, A.P., Quaipe, T., Van Bodegom, P.M., De Kauwe, M.G., Keenan, T.F., Joiner, J., Lomas, M.R., Macbean, N., Xu, C., Yang, X., 2017. The impact of alternative trait-scaling hypotheses for the maximum photosynthetic carboxylation rate (Vc,max) on global gross primary production. *New Phytol.* 215.
- Wang, L., Tian, F., Huang, K., Wang, Y., Wu, Z., Fensholt, R., 2020a. Asymmetric patterns and temporal changes in phenology-based seasonal gross carbon uptake of global terrestrial ecosystems. *Global Ecol. Biogeogr.* 29 (6), 1020–1033.
- Wang, L., Zhu, H., Lin, A., Zou, L., Qin, W., Du, Q., 2017. Evaluation of the latest MODIS GPP products across multiple biomes using global eddy covariance flux data. *Remote Sens.* 9 (5), 418.
- Wang, S., Zhang, Y., Ju, W., Chen, J.M., Ciais, P., Cescatti, A., Sardans, J., Janssens, I.A., Wu, M., Berry, J.A., Campbell, E., Fernández-Martínez, M., Alkama, R., Sitch, S., Friedlingstein, P., Smith, W.K., Yuan, W., He, W., Lombardozzi, D., Kautz, M., Zhu, D., Lienert, S., Kato, E., Poulter, B., Sanders, T.G.M., Krüger, I., Wang, R., Zeng, N., Tian, H., Vuitchard, N., Jain, A.K., Wiltshire, A., Haverd, V., Goll, D.S., Peñuelas, J., 2020b. Recent global decline of CO₂ fertilization effects on vegetation photosynthesis. *Science* 370 (6522), 1295–1300.
- Wang, X., Qiu, B., Li, W., Zhang, Q., 2019. Impacts of drought and heatwave on the terrestrial ecosystem in China as revealed by satellite solar-induced chlorophyll fluorescence. *Sci. Total Environ.* 693, 133627.
- Wang, Y., Law, R., Pak, B., 2010. A global model of carbon, nitrogen and phosphorus cycles for the terrestrial biosphere. *Biogeosciences* 7 (7), 2261.
- Wei, Y., Liu, S., Huntzinger, D.N., Michalak, A.M., Viovy, N., Post, W.M., Schwalm, C.R., Schaefer, K., Jacobson, A.R., Lu, C., 2014. The North American carbon program multi-scale synthesis and terrestrial model intercomparison project - Part 2: environmental driver data. *Geosci. Model Dev.* 7, 2875–2893.
- White, M.A., Thornton, P.E., Running, S.W., Nemani, R.R., 2000. Parameterization and sensitivity analysis of the BIOME-BGC terrestrial ecosystem model: net primary production controls. *Earth Interact.* 4 (3), 1–85.
- Wolf, S., Keenan, T.F., Fisher, J.B., Baldocchi, D.D., Desai, A.R., Richardson, A.D., Scott, R.L., Law, B.E., Litvak, M.E., Brunzell, N.A., 2016. Warm spring reduced carbon cycle impact of the 2012 US summer drought. In: *Proceedings of the National Academy of Sciences*, 201519620.
- Wood, J.D., Griffis, T.J., Baker, J.M., Frankenberg, C., Verma, M., Yuen, K., 2017. Multiscale analyses of solar-induced fluorescence and gross primary production. *Geophys. Res. Lett.* 44 (1), 533–541.
- Wu, M., Scholze, M., Kaminski, T., Voßbeck, M., Tagesson, T., 2020. Using SMOS soil moisture data combining CO₂ flask samples to constrain carbon fluxes during 2010–2015 within a Carbon Cycle Data Assimilation System (CCDAS). *Remote Sens. Environ.* 240, 111719.
- Wu, X., Xiao, X., Zhang, Y., He, W., Wolf, S., Chen, J., He, M., Gough, C.M., Qin, Y., Zhou, Y., Doughty, R., Blanken, P.D., 2018. Spatiotemporal consistency of four gross primary production products and solar-induced chlorophyll fluorescence in response to climate extremes across CONUS in 2012. *J. Geophys. Res.: Biogeosciences* 123 (10), 3140–3161.
- Wu, Z., Ahlström, A., Smith, B., Ardö, J., Eklundh, L., Fensholt, R., Lehsten, V., 2017. Climate data induced uncertainty in model-based estimations of terrestrial primary productivity. *Environ. Res. Lett.* 12 (6), 064013.
- Xia, J., McGuire, A.D., Lawrence, D., Burke, E., Chen, G., Chen, X., Delire, C., Koven, C., MacDougall, A., Peng, S., Rinke, A., Saito, K., Zhang, W., Alkama, R., Bohn, T.J., Ciais, P., Decharme, B., Gouttevin, I., Hajima, T., Hayes, D.J., Huang, K., Ji, D., Krinner, G., Lettenmaier, D.P., Miller, P.A., Moore, J.C., Smith, B., Sueyoshi, T., Shi, Z., Yan, L., Liang, J., Jiang, L., Zhang, Q., Luo, Y., 2017. Terrestrial ecosystem model performance in simulating productivity and its vulnerability to climate change in the northern permafrost region. *J. Geophys. Res.: Biogeosciences* 122 (2), 430–446.
- Xiao, X., Zhang, Q., Braswell, B., Urbanski, S., Boles, S., Wofsy, S., Moore, B., III, Ojima, D., 2004. Modeling gross primary production of temperate deciduous broadleaf forest using satellite images and climate data. *Remote Sens. Environ.* 91 (2), 256–270.
- Xiao, Z., Liang, S., Jiang, B., 2017. Evaluation of four long time-series global leaf area index products. *Agric. For. Meteorol.* 246, 218–230.
- Zan, M., Zhou, Y., Ju, W., Zhang, Y., Zhang, L., Liu, Y., 2018. Performance of a two-leaf light use efficiency model for mapping gross primary productivity against remotely sensed sun-induced chlorophyll fluorescence data. *Sci. Total Environ.* 977–989 s 613–614.

- Zeng, N., Mariotti, A., Wetzal, P., 2005. Terrestrial mechanisms of interannual CO₂ variability. *Glob. Biogeochem. Cycles* 19 (1), GB1016.
- Zhang, L., Qiao, N., Huang, C., Wang, S., 2019a. Monitoring drought effects on vegetation productivity using satellite solar-induced chlorophyll fluorescence. *Remote Sens.* 11 (4), 378.
- Zhang, Y., Guanter, L., Berry, J.A., Joiner, J., van der Tol, C., Huete, A., Gitelson, A., Voigt, M., Köhler, P., 2014. Estimation of vegetation photosynthetic capacity from space-based measurements of chlorophyll fluorescence for terrestrial biosphere models. *Global Change Biol.* 20 (12), 3727–3742.
- Zhang, Y., Guanter, L., Berry, J.A., Tol, C.V.D., Yang, X., Tang, J., Zhang, F., 2016a. Model-based analysis of the relationship between sun-induced chlorophyll fluorescence and gross primary production for remote sensing applications. *Remote Sens. Environ.* 187, 145–155.
- Zhang, Y., Guanter, L., Joiner, J., Song, L., Guan, K., 2018a. Spatially-explicit monitoring of crop photosynthetic capacity through the use of space-based chlorophyll fluorescence data. *Remote Sens. Environ.* 210, 362–374.
- Zhang, Y., Joiner, J., Gentile, P., Zhou, S., 2018b. Reduced solar-induced chlorophyll fluorescence from GOME-2 during Amazon drought caused by dataset artifacts. *Global Change Biol.* 24 (6), 2229–2230.
- Zhang, Y., Xiao, X., Jin, C., Dong, J., Zhou, S., Wagle, P., Joiner, J., Guanter, L., Zhang, Y., Zhang, G., 2016b. Consistency between sun-induced chlorophyll fluorescence and gross primary production of vegetation in North America. *Remote Sens. Environ.* 183, 154–169.
- Zhang, Y., Xiao, X., Wu, X., Zhou, S., Zhang, G., Qin, Y., Dong, J., 2017. A global moderate resolution dataset of gross primary production of vegetation for 2000–2016. *Sci. Data* 4, 170165.
- Zhang, Z., Chen, J.M., Guanter, L., He, L., Zhang, Y., 2019b. From canopy-leaving to total canopy far-red fluorescence emission for remote sensing of photosynthesis: first results from TROPOMI. *Geophys. Res. Lett.* 46 (21), 12030–12040.
- Zhou, S., Zhang, Y., Caylor, K.K., Luo, Y., Xiao, X., Ciais, P., Huang, Y., Wang, G., 2016. Explaining inter-annual variability of gross primary productivity from plant phenology and physiology. *Agric. For. Meteorol.* 226–227, 246–256.
- Zhu, H., Lin, A., Wang, L., Xia, Y., Zou, L., 2016. Evaluation of MODIS gross primary production across multiple biomes in China using eddy covariance flux data. *Remote Sens.* 8 (5), 395.
- Zscheischler, J., Mahecha, M.D., Von Buttlar, J., Harmeling, S., Jung, M., Rammig, A., Randerson, J.T., Schölkopf, B., Seneviratne, S.I., Tomelleri, E., 2014. A few extreme events dominate global interannual variability in gross primary production. *Environ. Res. Lett.* 9 (9), 035001.